Citation
Yuan, C. and Chen, W. and Pham, T.M. and Hao, H. and Cui, J. and Shi, Y. 2020. Influence of concrete strength on dynamic interfacial fracture behaviour between fibre reinforced polymer sheets and concrete. Engineering Fracture Mechanics. 229: ARTN 106934. http://doi.org/10.1016/j.engfracmech.2020.106934

Influence of concrete strength on dynamic interfacial fracture behaviour between fibre reinforced polymer sheets and concrete

Cheng Yuan[1], Wensu Chen[1]*, Thong M. Pham[1], Hong Hao[1]*, Jian Cui[2], Yanchao Shi[2]

[1]*Centre for Infrastructural Monitoring and Protection, School of Civil and Mechanical Engineering, Curtin University, Australia*

[2]*Tianjin University and Curtin University Joint Research Center of Structure Monitoring and Protection, School of Civil Engineering, Tianjin University, China*

*Corresponding Authors: wensu.chen@curtin.edu.au (W. Chen), hong.hao@curtin.edu.au (H. Hao).

Abstract

This study experimentally investigates the effect of concrete strength on the dynamic interfacial bond behaviour between basalt fibre reinforced polymer (BFRP) sheets and concrete under different loading speeds (i.e. 8.33E-6 m/s, 0.1 m/s, 1 m/s, 3 m/s, 5 m/s, and 8 m/s) by using single-lap shear tests. Three concrete strengths (i.e. C20, C30, and C40) were considered to examine the influence of concrete strength and strain rate on the interfacial bond-slip responses under dynamic loadings. The test results including the strain distributions, interfacial fracture energy, and bond-slip response were evaluated and discussed. The test results showed that the BFRP-concrete interface exhibited sensitivity to strain rate and the bond strength and interfacial shear stress increased with strain rate. Compared with high strength concrete, low strength concrete showed higher strain rate sensitivity, which is induced by the different interfacial fracture mechanisms under different strain rates. Empirical bond-slip model incorporating the effects of concrete strength and strain rate was proposed based on fracture mechanics.

Keywords: Bond-slip; Strain rate; Basalt fibre reinforced polymer (BFRP); Dynamic test.

1. Introduction

Reinforced concrete (RC) structures may experience extreme loading conditions, such as seismic, impact, and blast loadings, during their service life [1]. Numerous studies stated that existing RC structures need to be strengthened to resist these extreme loads [2]. Concrete exhibits sensitivity to high loading rates. It is a strain rate dependent material with respect to the compressive and tensile strengths and Young's modulus. The cause of strain rate in concrete is induced by the viscoelastic behaviour and time-dependent micro crack growth of the cement paste [3].

Fibre-reinforced polymer (FRP) sheet is widely utilized as strengthening as well as rehabilitating material due to its high strength to weight ratio, great corrosion resistance and ease of application [4, 5]. Externally bonded (EB) FRP composite is a very common method for strengthening RC structures [6, 7]. Numerous investigations have been carried out on the load-carrying capacity of EB FRP-strengthened RC elements, such as RC beams and slabs [8-11]. Previous studies have shown that FRP debonding which is a premature failure mode has detrimental effects on the EB FRP-strengthened RC structures [5, 12]. To investigate the debonding mechanism, various testing methods, such as single/double-lap shear tests, have been used [13, 14].

Numerous analytical models have been proposed to estimate the bond strength and shear stress in the literature [15, 16]. The codes and design guides, such as ACI 440.2R [17], HB 305 [18], fib Bulletin 14 [19], and CNR-DT200 [20], provide design procedures for practical engineering applications. However, most of the available models were proposed based on the quasi-static loading condition. Since the interfacial bond characteristics between FRP and concrete under dynamic loadings were different from those under quasi-static loadings [21], some experimental investigations have been carried out to unveil the interfacial bond behaviour between FRP and concrete subjected to dynamic loadings. The experimental study by Shi et al.

[22] reported that the interfacial bond was strain rate dependent and the interfacial fracture energy and peak shear stress increased with strain rate. The peak strain rate in the tests by Shi et al. [22] was around $0.1s^{-1}$. Shen et al. [23] carried out experimental studies on the strain rate effect on the bond performance with the strain rate up to 0.63 s^{-1} and reported that the effective bond length decreased with the increase of strain rate and the corresponding model for predicting the effective bond length was established. Based on Shen et al.'s test results [23], Antonio et al. [24] proposed a modified Duvant-Lions zero-thickness interface model to simulate the strain rate effect on the interfacial bond. Huo et al. [25] found that the interface was sensitive to strain rate through impact tests on CFRP-strengthened RC beams and the corresponding strain rate was up to 4.90 s^{-1}. Salimian et al. [26] conducted debonding tests to exam the loading rate effect on the interfacial bond capacities between CFRP and concrete and reported that specimens with lower concrete strength showed more sensitivity to loading rate. To sum up, the strain rate in the literature on bond performance was up to 4.90 s^{-1} and the testing results are insufficient to reflect the strain rate effect for the blast and impact scenarios, which have the corresponding strain rate up to hundreds per second.

In this study, single-lap shear tests at different loading speeds of $8.33E^{-6}$ m/s, 0.1 m/s, 1 m/s, 3 m/s, and 8 m/s were carried out to achieve strain rates ranging between $2.50E^{-5}$ s^{-1} and 175.65 s^{-1}. Experimental results including debonding failure modes, strain distributions, and bond-slip relationship were compared and discussed. The effect of strain rate was evaluated by comparing the results of dynamic tests and static tests. The dynamic bond-slip model was established to estimate the bond strength for the FRP-concrete interface based on fracture mechanics.

2. Experimental program

2.1 Material properties

Concrete blocks with 150 x 150 x 300 mm in dimension were prepared for the tests. The compressive strengths of three series of concrete (C20, C30 and C40) were respectively 22.40 MPa, 30.14 MPa, and 42.34 MPa and the corresponding splitting tensile strengths were 2.11 MPa, 3.12 MPa, and 4.13 MPa, respectively. The coarse aggregate size of 5-20 mm was used in the test program. The FRP coupon tests on uni-directional basalt fibre (BFRP) sheets with nominal thickness of 0.12 mm were conducted to obtain the rupture tensile strength, rupture strain, and elastic modulus, which were 1333 MPa, 0.19%, 72 GPa, respectively.

2.2 Test setup

The test setup and experimental facilities are shown in Figure 1. The dynamic testing machine (ISTRON® VHS 160-20) controlled by high speed servo hydraulic was used to conduct dynamic single-lap shear tests. Constant speed in the range of 0.1 m/s to 25 m/s can be provided by this machine. The fast jaw was accelerated to the expected loading speed and gripped the specimen. The steel holding frame was properly designed rigid enough to hold a specimen to avoid any possible movement during the test. A high-speed camera with intensive lights was used to record the debonding process. The digital image correlation (DIC) technique was used to obtain the surface slip and strain by analysing the recorded successive digital images. This technique is able to provide a wide strain field of FRP sheets. To carry out the DIC analysis, each specimen with a white base and randomly distributed black speckles were prepared. The bonded region was selected as the region of interest (ROI), as shown in Figure 2.

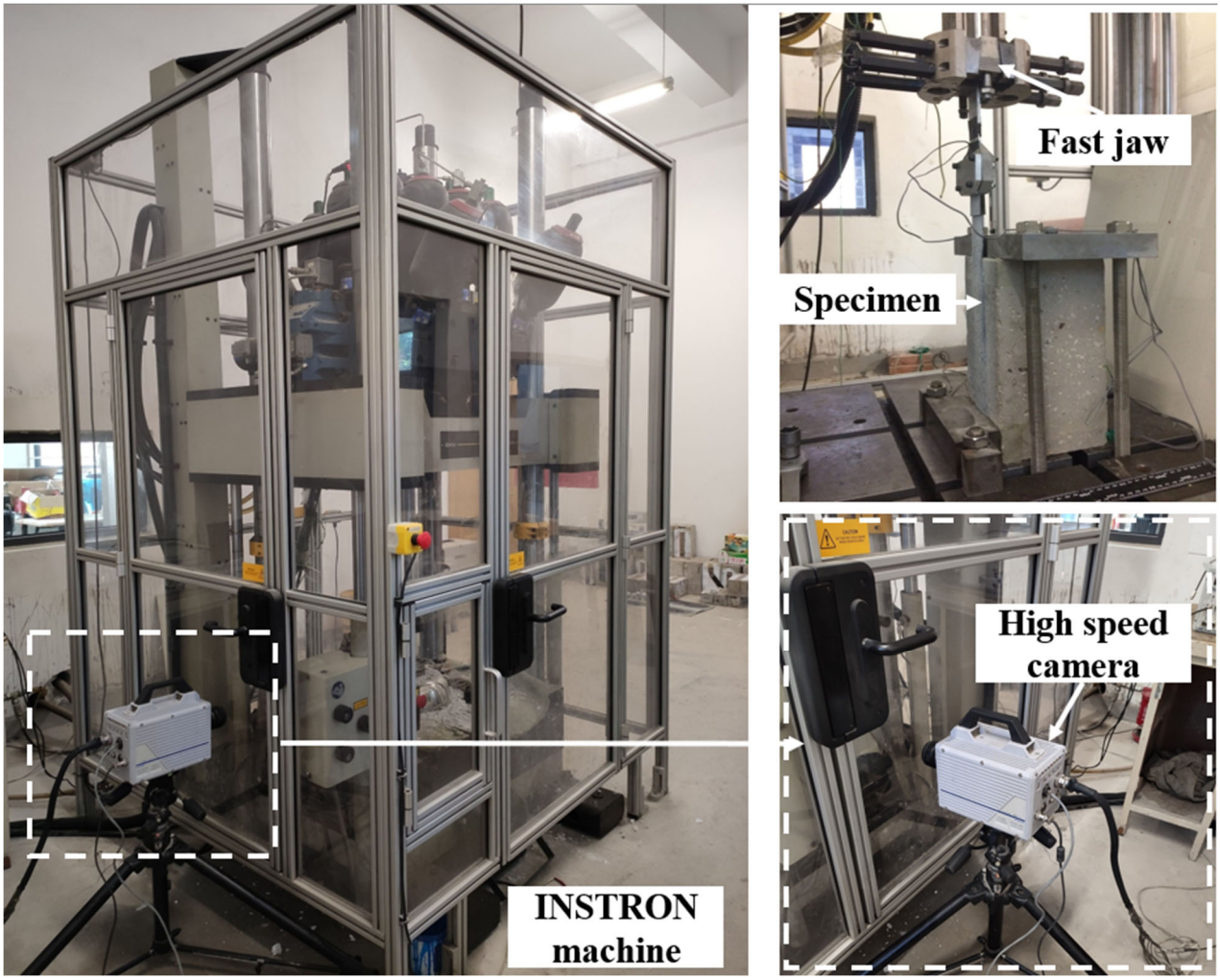

Figure 1. Experimental facilities

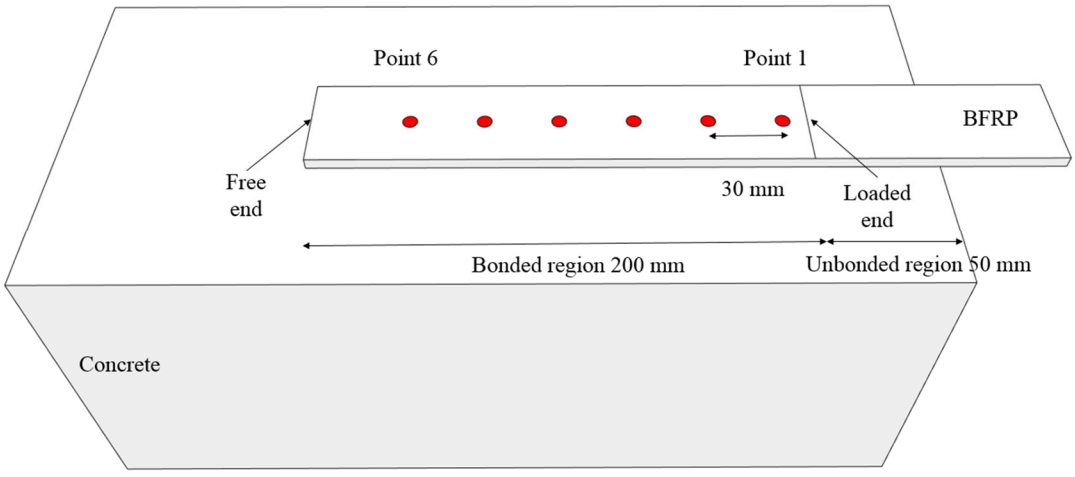

Figure 2. Specimen detail

3. Validation of dynamic stress equilibrium

As a non-contact measurement method, the accuracy of the DIC technique was carefully checked in the previous studies by the authors to obtain reliable test data [27-29]. In addition, experimental results of dynamic debonding tests are valid only when stress equilibrium is achieved. Therefore, the strain-time histories of the tested specimens are plotted to prove the dynamic stress equilibrium, as shown in Figure 3. Six tracking points (Points 1 to 6) along the centreline of FRP surface were selected to compare, as illustrated in Figure 2. Similar strain profiles were observed at different time instants and the strain developed a similar plateau, indicating uniform stress distribution. It is noted that the strain distributions of Point 1 and Point 6 are different from others since Point 1 is placed at the boundary of the bonded and unbonded region and Point 6 is located near the free end, which cannot develop the entire debonding process. It should be noted that specimen C20-1-2 refers to the specimen with compressive strength of 20 MPa subjected to the dynamic loading speed of 1 m/s and the last digit refers to the specimen number, i.e., the second specimen in the group of three identical specimens.

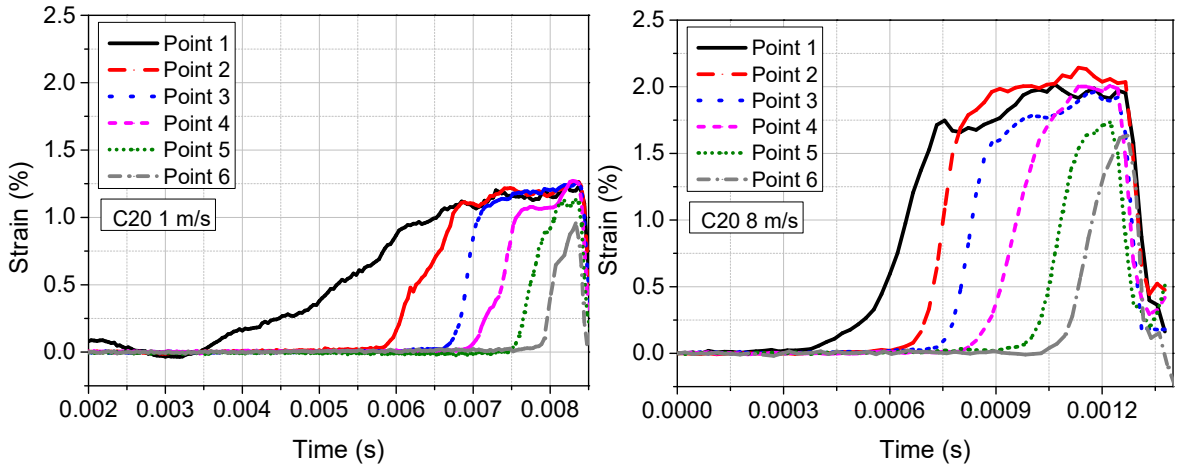

(a) C20-1-1 (b) C20-8-1

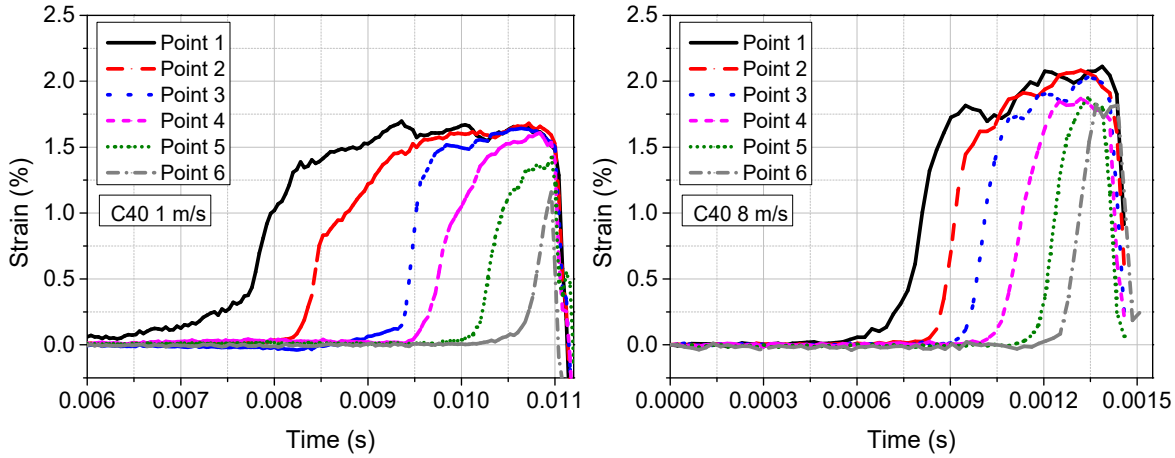

(c) C40-1-1 (d) C40-8-1

Figure 3. Strain time histories

The strain rate can be derived from differentiation of strain time history. Figure 4 illustrates the variation of the strain rate along the bonded length at different time instants. The peak strain rate was selected as the measured strain rate for each specimen. For instance, the peak strain rate for the specimen C40-8-1 was 161.18 s^{-1} and the maximum strain rate for the specimen C40-0.1-1 was 6.69 s^{-1}. The strain rate of each specimen is summarized in Table 1.

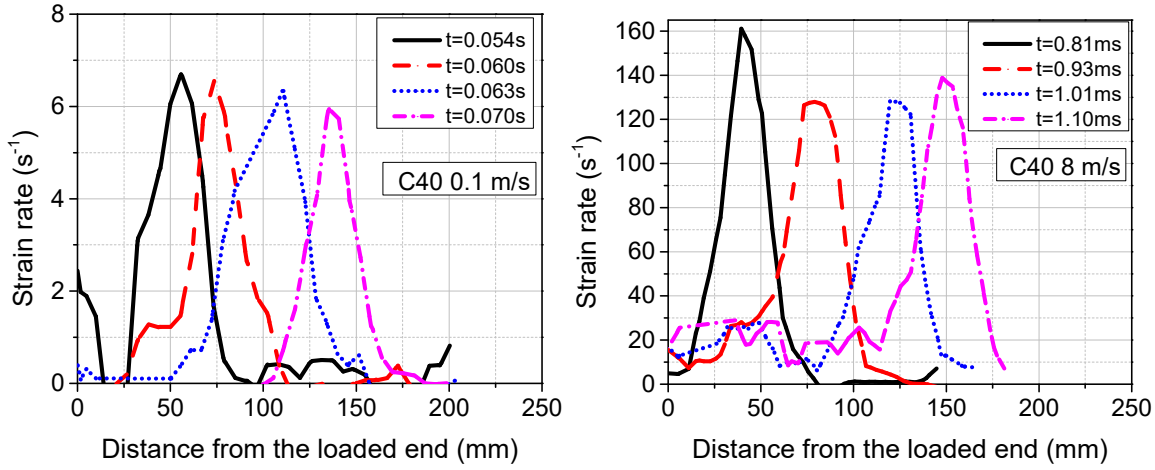

(a) C40-0.1-1 (b) C40-8-1

Figure 4. Strain rate distribution

4. Test results and discussions

4.1 Debonding load and failure mode

Table 1 summarizes the test results of the debonding load and failure modes. The debonding load in average increased with the rising strain rate irrespective of the concrete strength, as shown in Figure 5. The specimens with the highest concrete strength (i.e. C40) showed the greatest bond strength at all the loading speeds. Previous studies have also reported that the debonding load enhanced with strain rate [30, 31]. When subjected to the dynamic loading rate of 8 m/s, all the specimens experienced a minor difference in the debonding load. However, the specimens with the lowest concrete strength (i.e. C20) showed the highest increment on debonding load, which is shown in Figure 6. Compared to the quasi-static testing data, an increment of 129.14% is obtained for the specimen C20-8 at the dynamic testing of 8 m/s. Specimen C40-8 shows the lowest dynamic increment of 63.66% as compared to the specimens with lower concrete strength at the same speed. This indicates that the strain rate effect on the bond strength of the specimens is concrete strength dependent. The specimens with the concrete strength of about 20 MPa are most strain rate sensitive. However, mixed observations for specimens with concrete strength of about 30 MPa and 40 MPa were obtained, i.e., the strain rate sensitivity of C30 specimens is not always higher than that of C40 specimens. The possible reason is due to the different bond fracture mechanisms and detailed explanations are given in section 4.2.

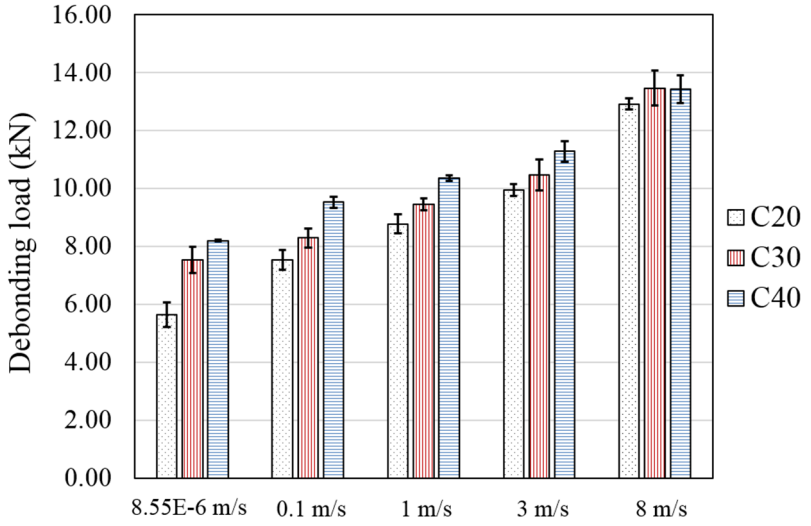

Figure 5. Debonding load of specimens

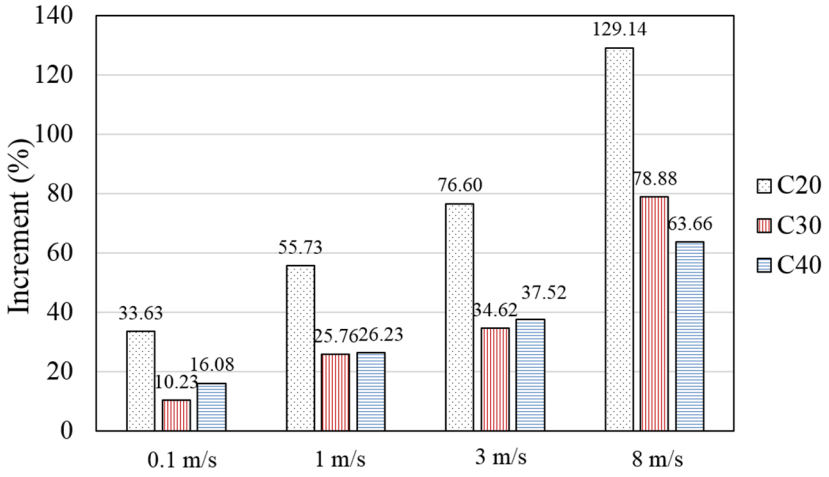

Figure 6. Increment ratio of debonding load

The enhanced dynamic interfacial bond strength is attributed to the enhanced concrete tensile strength with strain rate. Previous studies [32, 33] have demonstrated that both the compressive and tensile strength of concrete enhanced with strain rate and the corresponding enhancement of tensile strength varied from 10% to 170% when strain rate increased from 10 s^{-1} to 100 s^{-1}. As the single-lap shear test method was employed in this test program, the interface between BFRP and concrete was subjected to shear stress through the adhesive layer or penetrated into the concrete layer [26]. It is well-known that concrete is strong in compression but weak in tension. Therefore, the fracture of concrete layer is normally governed by its tensile strength for single-lap shear tests. Under relatively low loading rates (less than 1 m/s), failure occurred

inside the concrete layer as a thin layer of concrete beneath the BFRP sheets was observed after the final detachment, as shown in Figure 7. Therefore, the interfacial bond strength should be mainly determined by the tensile strength of concrete.

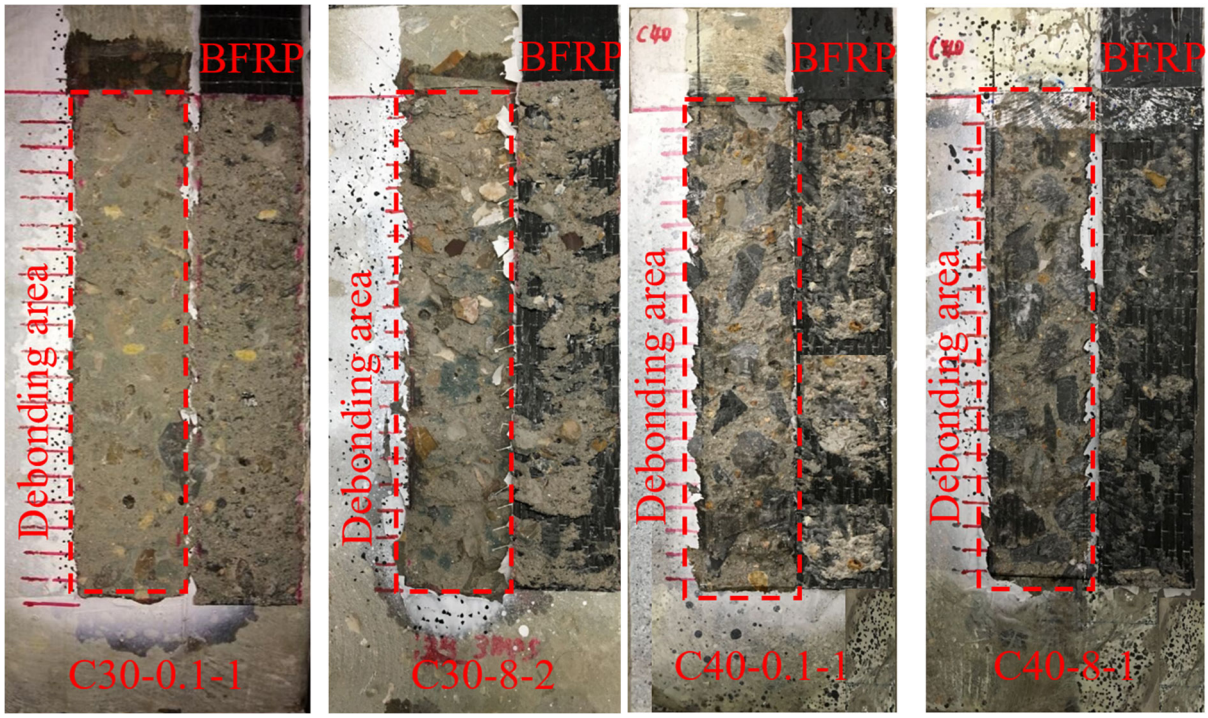

Figure 7. Typical failure modes

Meanwhile, a combined failure mode (i.e. C and CA) was observed when the testing velocity was over 3 m/s. The fracture interface shifted from concrete layer to the interface of concrete-adhesive. This is because the dynamic increase factor (DIF) of concrete in tension increased faster than the epoxy resin and there was not enough time for the cracks to develop in the concrete under high loading rate. The fracture at the adhesive interface layer was also observed in some cases when the speed was over 3 m/s. As the tensile strength of the adhesive is stronger than other interfaces, fracture of the adhesive layer resulted in a greater debonding load. Compared with high strength concrete specimens, specimen C20 was more sensitive to strain rate due to the highest increment in bond strength and concrete damage after debonding. It is reasonable since the literature has shown that lower concrete strength is more sensitive to strain

Table 1. Specimen details and test results

Specimen ID	f_c (MPa)	f_t (MPa)	Loading speed (m/s)	Strain rate (s^{-1})	P_u (kN)	ε_u (%)	τ_m (MPa)	s_o (mm)	G_f (N/mm)	$f_{t,d}$ (MPa)	$G_{f,pre.}$ (N/mm)	$\tau_{m,pre.}$ (MPa)	$\varepsilon_{u,pre.}$ (%)	$P_{u,pre.}$ (kN)	Failure mode
C20-QS-1	22.40	2.11	8.33E-6	2.50E-5	5.94	0.859	1.97	0.098	0.63	2.11	0.73	3.05	0.912	6.39	C
C20-QS-2	22.40	2.11	8.33E-6	2.50E-5	5.34	0.917	1.56	0.111	0.51	2.11	0.73	3.05	0.912	6.39	C
C20-0.1-1	22.40	2.11	0.1	4.57	7.19	1.040	4.16	0.131	0.92	6.71	1.30	5.45	1.218	8.54	C
C20-0.1-2	22.40	2.11	0.1	3.91	7.56	1.094	3.92	0.118	1.02	6.50	1.28	5.36	1.209	8.47	C
C20-0.1-3	22.40	2.11	0.1	3.76	7.86	1.137	4.08	0.102	1.10	6.45	1.27	5.34	1.206	8.45	C
C20-1-1	22.40	2.11	1	33.38	8.75	1.196	5.23	0.111	1.37	9.34	1.53	6.43	1.323	9.27	C
C20-1-2	22.40	2.11	1	29.79	9.12	1.319	4.54	0.124	1.48	9.19	1.52	6.37	1.318	9.23	C
C20-1-3	22.40	2.11	1	30.26	8.48	1.227	4.98	0.097	1.28	9.21	1.52	6.38	1.318	9.24	C
C20-3-1	22.40	2.11	3	52.36	9.91	1.434	7.19	0.111	1.75	9.94	2.04	6.63	1.524	10.68	C
C20-3-2	22.40	2.11	3	49.85	9.78	1.415	6.79	0.109	1.71	9.87	2.03	6.61	1.522	10.66	C
C20-3-3	22.40	2.11	3	45.23	10.19	1.474	7.41	0.101	1.85	9.74	2.02	6.56	1.517	10.63	C/CA
C20-8-1	22.40	2.11	8	147.37	12.84	1.858	10.12	0.112	2.94	11.30	2.17	7.07	1.574	11.03	C/CA
C20-8-2	22.40	2.11	8	151.74	12.79	1.850	9.31	0.104	2.92	11.34	2.17	7.08	1.575	11.04	C/CA
C20-8-3	22.40	2.11	8	124.60	13.14	1.901	9.47	0.103	3.08	11.08	2.15	7.00	1.566	10.98	C/CA
C30-QS-1	30.14	3.12	8.33E-6	2.50E-5	7.85	1.105	2.92	0.113	0.96	3.12	0.89	3.71	1.006	7.05	C
C30-QS-2	30.14	3.12	8.33E-6	2.50E-5	7.21	1.057	3.34	0.128	0.93	3.12	0.89	3.71	1.006	7.05	C
C30-0.1-1	30.14	3.12	0.1	4.91	8.38	1.153	5.19	0.119	1.25	10.06	1.59	6.67	1.348	9.45	C
C30-0.1-2	30.14	3.12	0.1	4.31	7.94	1.118	4.89	0.121	1.12	9.81	1.57	6.58	1.339	9.39	C
C30-0.1-3	30.14	3.12	0.1	4.21	8.58	1.208	5.41	0.118	1.31	9.76	1.57	6.57	1.338	9.37	C
C30-1-1	30.14	3.12	1	25.90	9.27	1.263	6.69	0.119	1.53	13.31	1.83	7.67	1.446	10.13	C
C30-1-2	30.14	3.12	1	33.31	9.46	1.332	6.83	0.117	1.60	13.81	1.86	7.81	1.459	10.22	C
C30-1-3	30.14	3.12	1	29.56	9.68	1.292	6.89	0.115	1.67	13.57	1.85	7.75	1.453	10.18	C
C30-3-1	30.14	3.12	3	65.12	10.11	1.423	8.32	0.101	1.82	15.12	2.51	8.17	1.693	11.86	C/CA
C30-3-2	30.14	3.12	3	57.01	11.09	1.387	7.85	0.121	2.19	14.86	2.49	8.10	1.686	11.81	C/CA
C30-3-3	30.14	3.12	3	60.75	10.21	1.437	8.19	0.103	1.86	14.98	2.50	8.14	1.689	11.84	C/CA
C30-8-1	30.14	3.12	8	155.55	14.07	1.981	10.21	0.111	3.53	16.82	2.65	8.62	1.739	12.18	C/CA
C30-8-2	30.14	3.12	8	175.65	13.47	1.896	9.82	0.106	3.24	17.06	2.67	8.68	1.745	12.23	C/CA
C30-8-3	30.14	3.12	8	150.76	12.87	1.812	9.39	0.102	2.95	16.76	2.64	8.61	1.737	12.17	C/CA
C40-QS-1	42.34	4.13	8.33E-6	2.50E-5	8.23	1.389	5.21	0.145	1.03	4.13	1.02	4.27	1.079	7.56	C
C40-QS-2	42.34	4.13	8.33E-6	2.50E-5	8.19	1.260	4.45	0.138	1.07	4.13	1.02	4.27	1.079	7.56	C
C40-0.1-1	42.34	4.13	0.1	6.69	9.55	1.552	6.28	0.129	1.46	13.58	1.85	7.75	1.453	10.18	C
C40-0.1-2	42.34	4.13	0.1	7.24	9.32	1.447	5.78	0.121	1.39	14.32	1.90	7.96	1.472	10.32	C
C40-0.1-3	42.34	4.13	0.1	4.03	9.72	1.491	6.54	0.124	1.52	12.81	1.80	7.52	1.432	10.03	C
C40-1-1	42.34	4.13	1	56.68	10.47	1.555	8.75	0.118	1.76	19.65	2.22	9.32	1.593	11.17	C
C40-1-2	42.34	4.13	1	33.45	10.26	1.709	9.05	0.117	1.69	18.29	2.15	8.99	1.565	10.97	C
C40-1-3	42.34	4.13	1	40.54	10.36	1.644	8.49	0.115	1.72	18.78	2.17	9.11	1.576	11.04	C/CA
C40-3-1	42.34	4.13	3	85.69	11.42	1.618	9.17	0.117	2.09	20.72	2.94	9.57	1.832	12.84	C/CA
C40-3-2	42.34	4.13	3	79.03	11.56	1.667	8.98	0.121	2.15	20.51	2.92	9.52	1.827	12.80	C/CA
C40-3-3	42.34	4.13	3	81.27	10.89	1.844	8.91	0.109	1.90	20.59	2.93	9.54	1.829	12.82	C/CA
C40-8-1	42.34	4.13	8	161.18	13.81	1.957	10.78	0.128	3.40	22.36	3.05	9.94	1.867	13.08	C/CA
C40-8-2	42.34	4.13	8	145.53	12.89	1.827	9.98	0.104	2.96	22.09	3.03	9.88	1.861	13.04	C/CA
C40-8-3	42.34	4.13	8	157.48	13.61	1.929	10.06	0.119	3.30	22.30	3.05	9.93	1.866	13.07	C/CA

Note: *C* refers to the debonding in the concrete layer, CA means the debonding in the concrete-adhesive layer, $f_{t,d}$ is the dynamic tensile strength of concrete, $G_{f,pre.}$ is the predicted interfacial fracture energy, $\tau_{m,pre.}$ is the predicted interfacial peak shear stress, $\varepsilon_{u,pre.}$ is the predicted ultimate debonding strain, $P_{u,pre.}$ is the predicted debonding load.

rate [26]. As shown in Figure 8, specimen C20-8-3 experienced significant damage due to the pull-out of coarse aggregates and fracture of mortar. The observed fracture propagated along the aggregate-to-mortar interface. This is due to the weakest interfacial transition zone (ITZ) caused by high ratio of aggregates and low ratio of cement used in the concrete mixture for C20. For the specimens with higher concrete strength, the damage of concrete was marginal at the dynamic testing of 8 m/s and only a flake of mortar fractured with the detachment of BFRP sheets, which is evidenced in Figure 7.

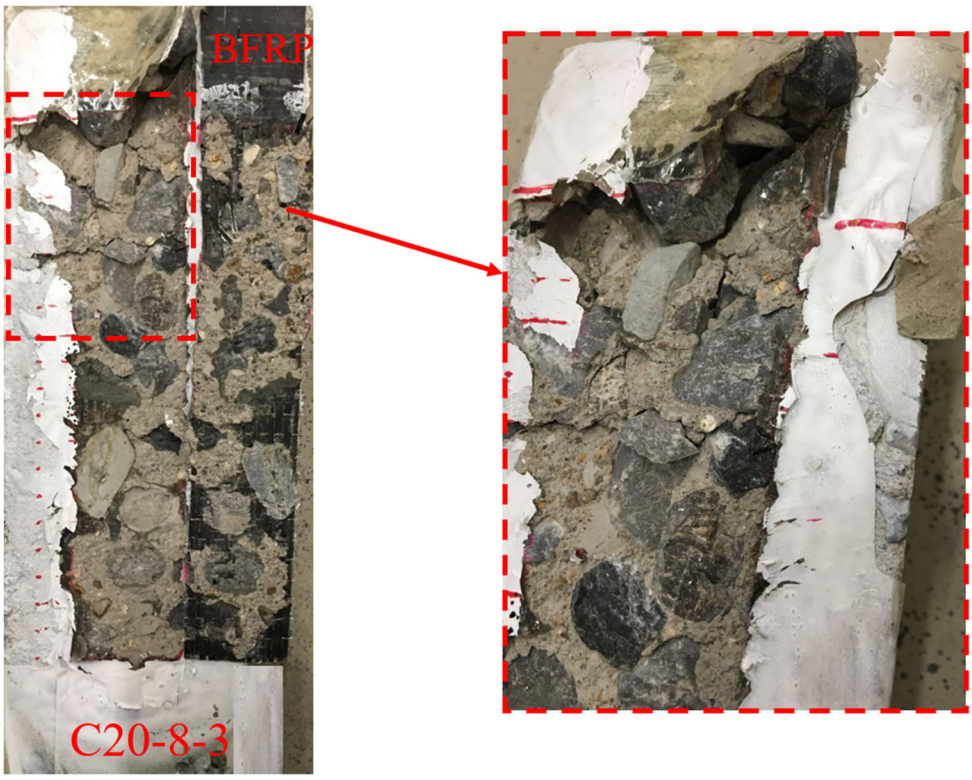

Figure 8. Fracture surface of C20-8-3

4.2 Strain distribution

To quantify the dynamic interfacial bond-slip responses, the strain profiles along the centreline of the BFRP sheets at different loading levels are plotted in Figure 9. It is found that the debonding strain for all the tested specimens increased with strain rate irrespective of the concrete strength. After reaching the initial debonding load P_u, the ultimate strain was almost constant and maintained its "*Z*" shape when the debonding process propagated. To present the

strain distributions at different time instants, four loading stages after the initial debonding load P_u were selected and contrasted. Different from the specimens with a low concrete strength, specimen C40 showed the highest ultimate debonding strain when the testing speed was less than 3 m/s. This is because higher concrete strength resulted in stronger interface and larger deformation of BFRP sheets to resist higher interfacial bond strength. However, when the testing velocity was over 3 m/s, the debonding strain showed insignificant difference for specimens with different strengths. This is because the debonding strain was governed by the response of the interface rather than concrete. Therefore, the concrete strength did not considerably affect the debonding strain. Instead, the epoxy strength governed the fracture process and thus the debonding strain. All the specimens in this study used the same epoxy resin so that similar debonding strain was expected if the failure occurred at the interface.

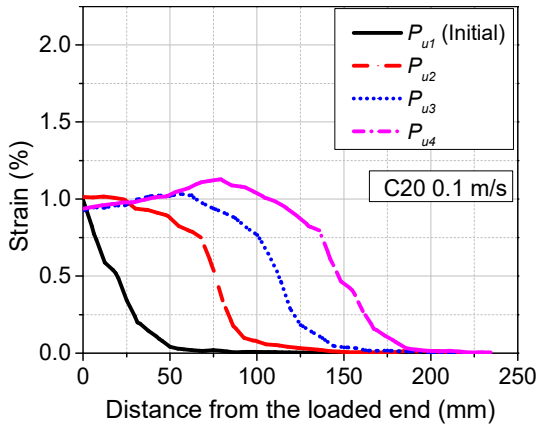

(a) C20-0.1-1

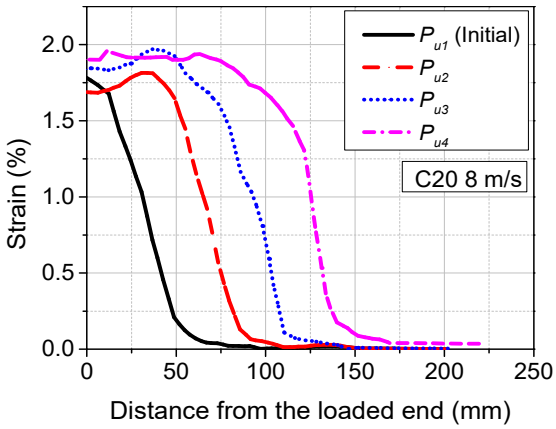

(b) C20-8-1

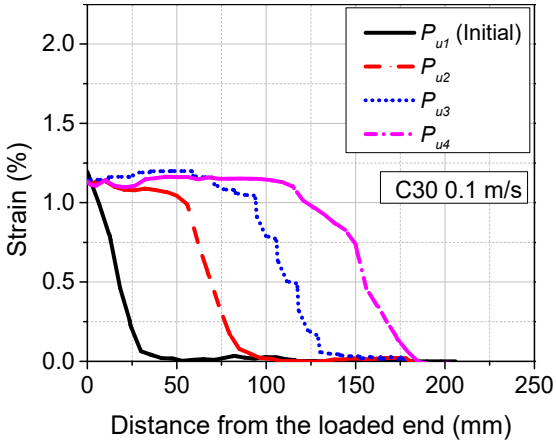

(c) C30-0.1-1

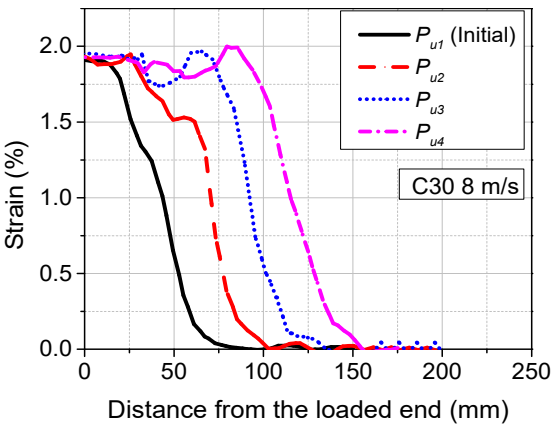

(d) C30-8-1

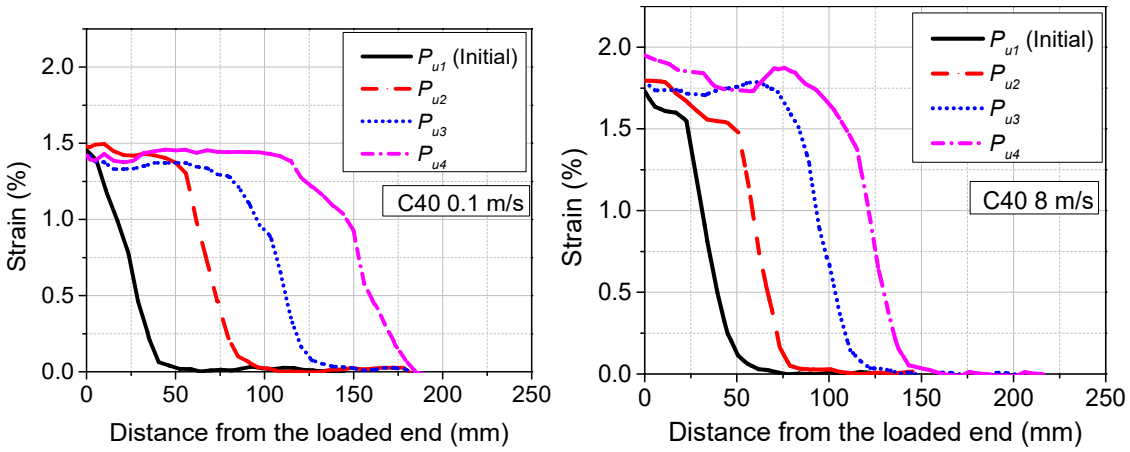

(e) C40-0.1-1 (f) C40-8-1

Figure 9. Typical strain profile

4.3 Experimental bond-slip curves

The typical shear stress and slip curves are plotted in Figure 10. To obtain accurate and reliable results, five different loading stages within the plateau region of the load-slip curves after the initial debonding stage were selected to obtain the shear stress and slip curves, i.e., 60 mm, 90 mm, 120 mm, 150 mm and 180 mm, which refers to the available stress transfer length along the BFRP sheets. The obtained shear stress and the corresponding shear slip are the average values of five loading stages. All the tested specimens showed similar bond-slip profile with an ascending branch and a descending branch. The shear stress increased firstly with the applied load. After reaching the peak shear stress, the degradation of shear stress initiated until the final detachment. A relatively small shear slip developed in the ascending branch, which was caused by the elastic linear stage of the BFRP-to-concrete interface [34, 35]. A larger shear slip was observed for the descending branch, which was resulted from the interfacial softening stage [36]. The shear stress (τ) and shear slip (s) can be derived by using the equations as follows:

$$\tau(x) = E_f t_f \frac{d\varepsilon}{dx} \quad (1)$$

$$s(x) = \int \varepsilon dx \quad (2)$$

in which E_f is the elastic modulus of BFRP sheets, t_f is the thickness of a BFRP sheet, ε is the BFRP strain, $\tau(x)$ is the shear stress along the bonded area, and s(x) is the shear slip along the bonded area.

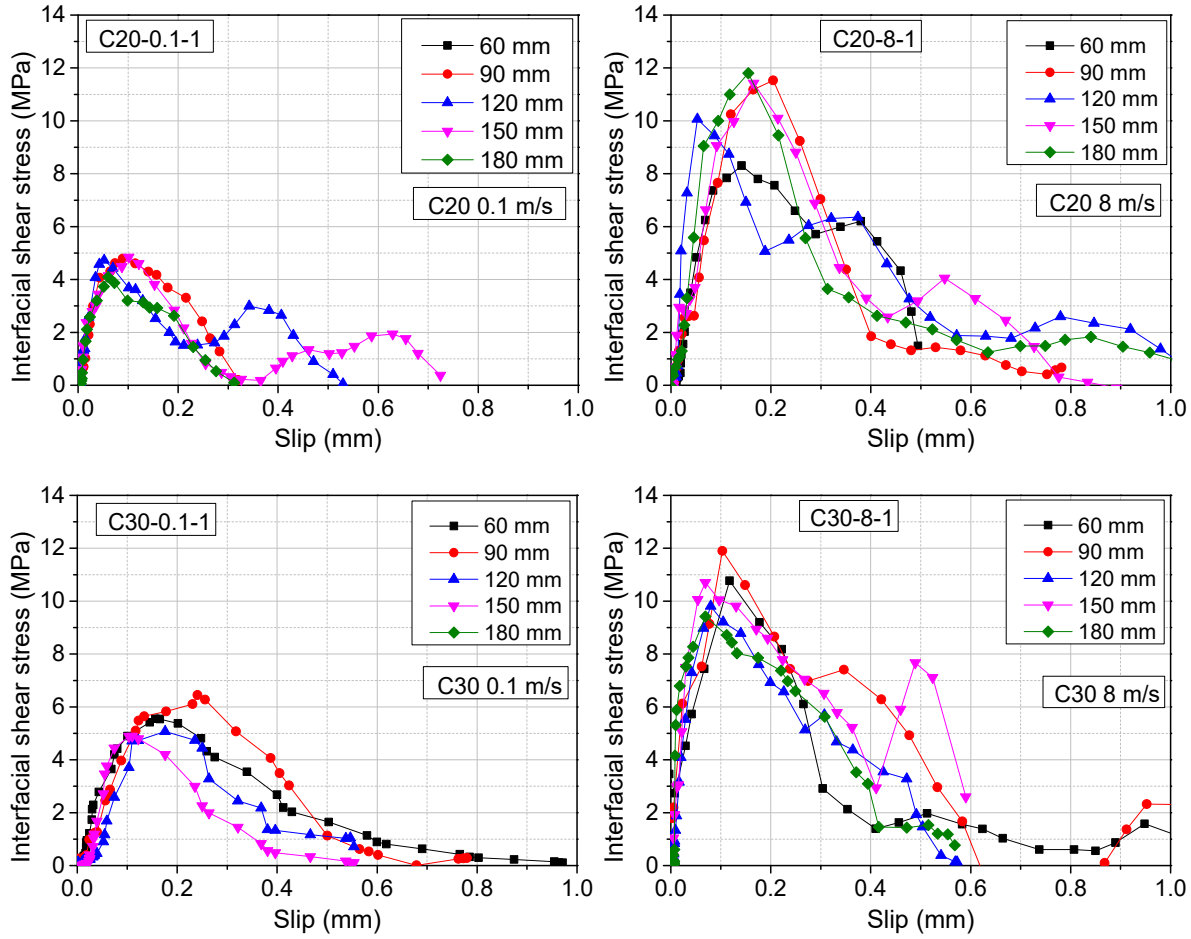

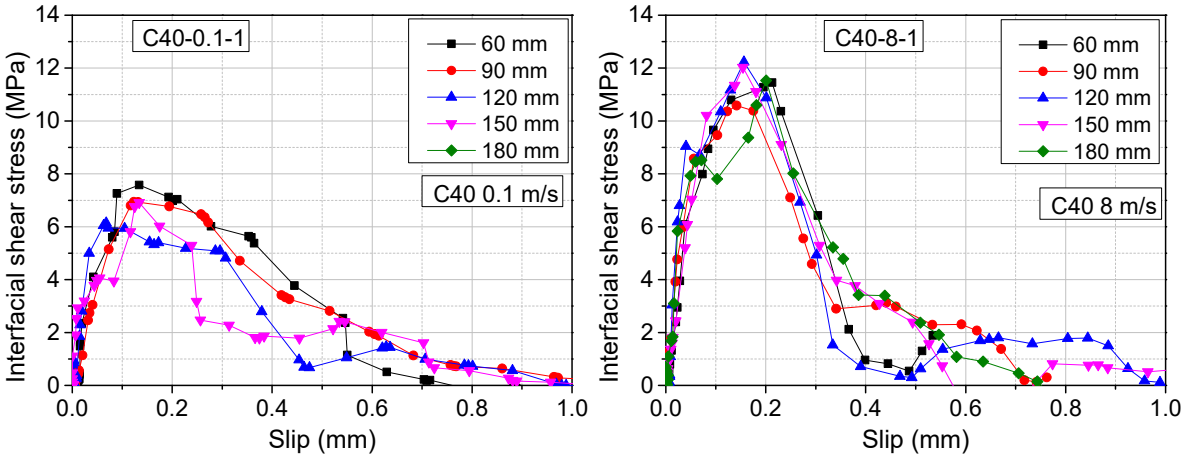

Figure 10. Typical shear stress and slip curves

It is observed that the peak shear stress increased significantly with strain rate, as shown in Figure 11. For the specimens with a lower concrete strength, specimen C20-QS showed the lowest interfacial shear stress, which was 1.77 MPa and the corresponding shear slip was 0.105 mm. The peak shear stress for specimen C30-QS and C40-QS was 3.13 MPa and 4.83 MPa and the corresponding slip was 0.121 mm and 0.142 mm, respectively, indicating that shear slip increased with the concrete strength. These observations are consistent with those reported in previous studies that the shear slip was proportional to the concrete strength [35, 37]. The testing results show that the shear slip decreased with strain rate. The measured shear slips for specimens C20-8, C30-8, and C40-8 at the dynamic testing of 8 m/s were 0.106 mm, 0.106 mm, and 0.117 mm, respectively. Additionally, specimen C20 showed the highest increment in the peak shear stress, which increased by up to 453.35% at the dynamic testing of 8 m/s. However, specimen C40 only increased by up to 112.01% at the same testing speed. This indicates that the specimens with lower concrete strength showed greater strain rate sensitivity in interfacial shear stress while specimens with higher concrete strength exhibited less strain rate sensitivity and greater shear resistance. It is worth noting that the interfacial peak shear stress of specimens with different concrete strengths exhibited large variations but this

variation became small at a high loading rate, i.e. 8 m/s. The reason for this phenomenon was due to the failure shifting from concrete-dominant to interface-dominant.

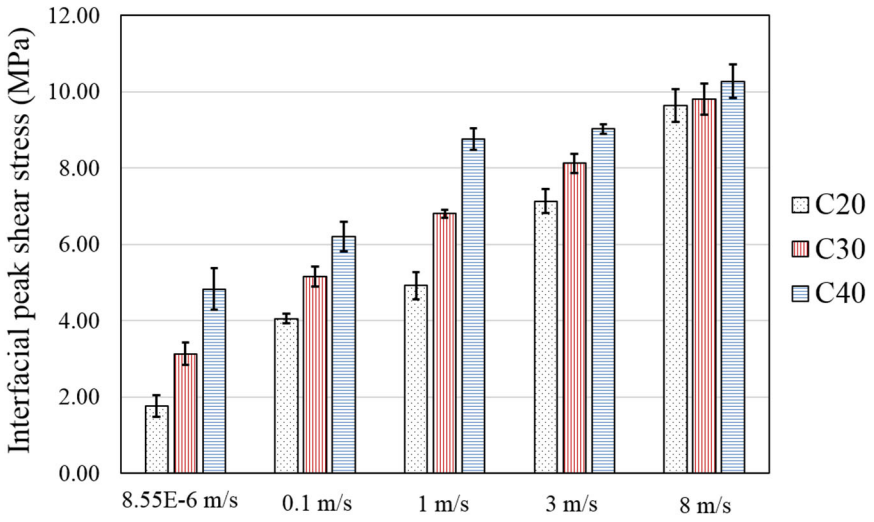

Figure 11. Comparison of interfacial shear stress

The enclosed area of the bond-slip curve represents the fracture energy G_f. It is observed that the interfacial fracture energy increased significantly with strain rate, especially for the specimens with a low concrete strength. Figure 12 (a) plots the average result of each testing group. The interfacial fracture energy of specimen C20-QS was the lowest at 0.67 N/mm while the value for the specimen C40-QS was 1.59 N/mm, indicating that the specimens with higher concrete strength released greater energy during the debonding process. As the specimen with the lowest concrete strength was more sensitive to strain rate, the interfacial fracture energy exhibited a higher increment. The interfacial fracture energy of specimen C20-8 raised by 423.63% when the loading speed was increased to 8 m/s. However, specimen C40-8 showed the lowest increment in fracture energy which was 206.96% at the highest loading speed, as shown in Figure 12 (b). Additionally, specimens C30 and C40 exhibited a similar fracture energy under 8 m/s, indicating that the effect of strain rate on fracture energy was more significant than that of concrete strength when the loading speed was over 3 m/s. This is because the shifted debonding failure from concrete to the concrete-epoxy interface at a

relatively high strain rate due to the fact that the dynamic increase factor (DIF) of concrete in tension increased faster than the epoxy resin and there was insufficient time for the cracks to develop in concrete under high loading rate.

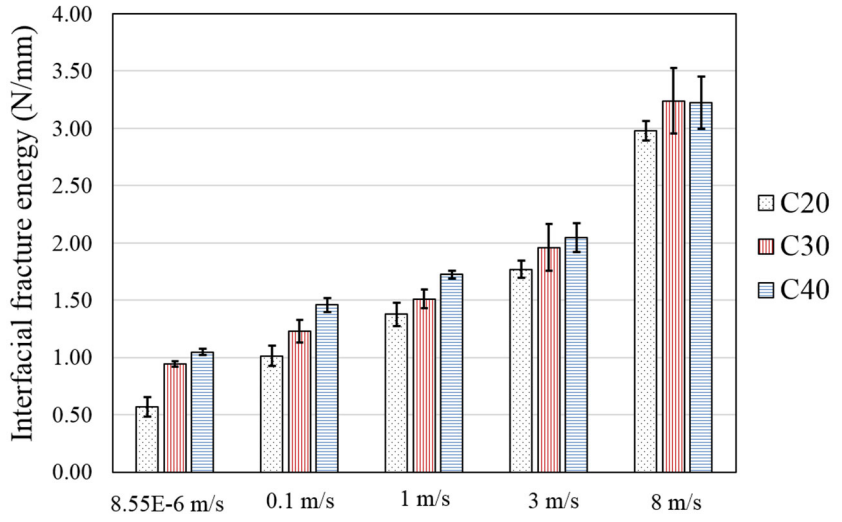

(a) Interfacial fracture energy vs. loading rate

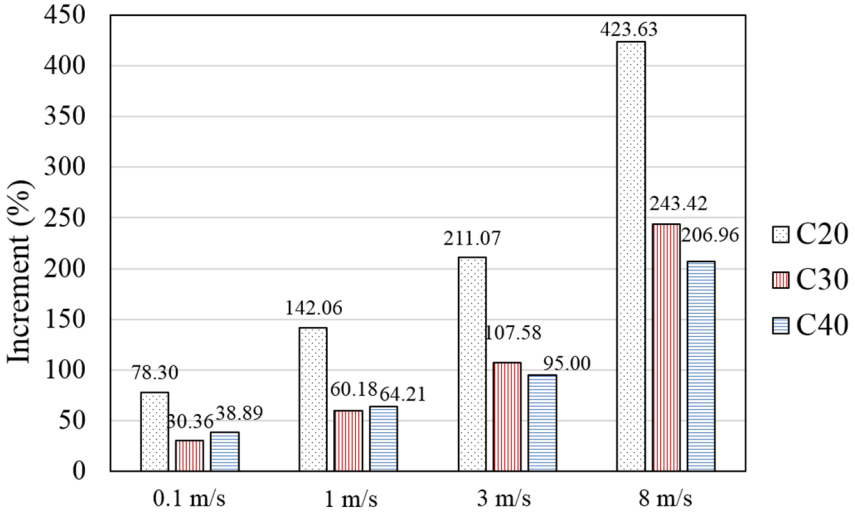

(b) Increment ratio of interfacial fracture energy

Figure 12. Test results of interfacial fracture energy

5. Analytical study of dynamic interfacial bond performance

Based on the shear stress-slip curves of the tested specimens under different loading speeds, an approximate triangle shape can be observed, as shown in Figure 10. For simplicity, a simplified bond-slip model is used to model the bond-slip relationship, as shown in Figure 13 (R). The

simplified bond-slip law coincides with the experimental shear stress and slip curve. The difference from the previous bond-slip law is that the linear ascending stage is separated by a turning point, which represents the change of the slope of the bond-slip response and this stage is referred as the hardening stage (i.e. stage II) in the previous studies [38, 39].

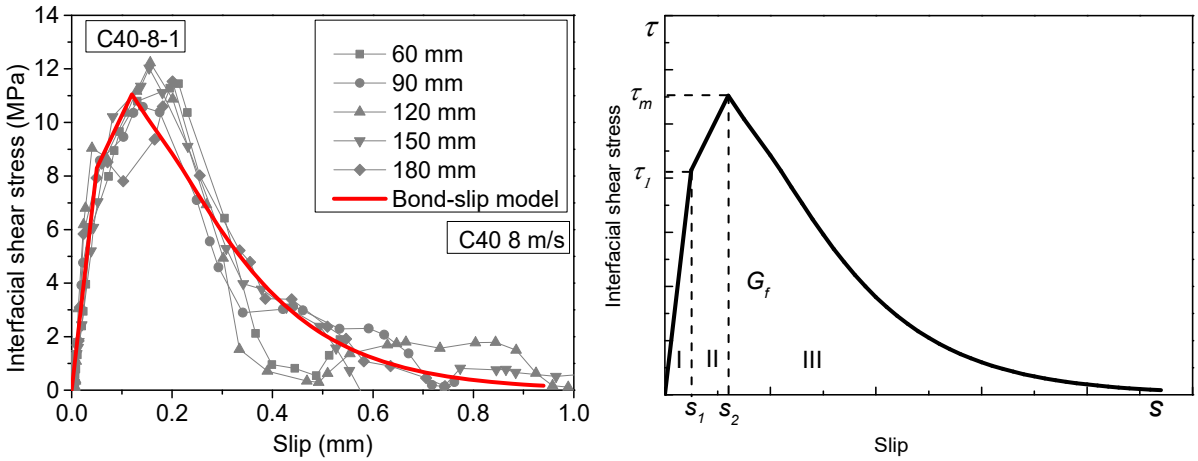

Figure 13. (L) Bond-slip curve of C40-8-1; (R) Simplified bond-slip law with hardening

The simplified bond-slip law includes three stages (I, II, and III) including: (I) linear-elastic stage when the shear slip increases to s_1; (II) linear hardening stage when the shear slip increased from s_1 to s_2 [38, 39]; and (III) softening stage where the shear stress degrades exponentially with the increased shear slip, as shown in Figure 13. The mathematical expressions for the simplified bond-slip model can be expressed as follows [38, 39]:

$$\tau(s)=\begin{cases}\tau_1\left(\dfrac{s}{s_1}\right) & s\le s_1\\ \dfrac{\tau_2-\tau_1}{s_2-s_1}s+\dfrac{\tau_1 s_2}{s_2-s_1}-\dfrac{\tau_2 s_1}{s_2-s_1} & s_1<s\le s_2\\ \tau_m e^{-\omega(s-s_2)} & s_2<s\le s_u\end{cases} \quad (3)$$

in which τ is the interfacial shear stress, s is the shear slip, and ω is the factor determining the shape of the softening stage.

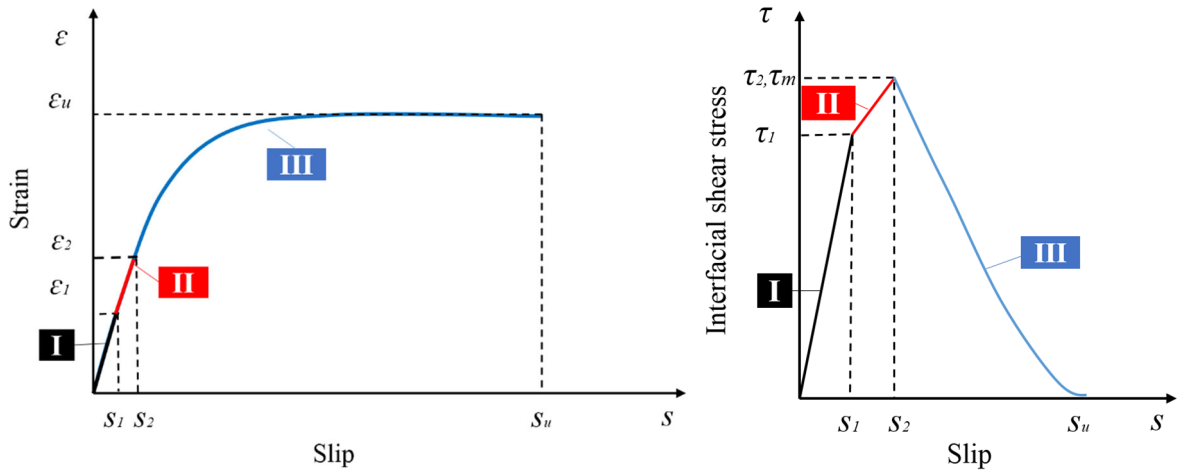

Figure 14. Determination of the bond-slip model

The bond-slip law is determined by some key parameters, i.e., τ_1, τ_2, τ_m, s_1, s_2, s_u, and ω. Meanwhile, the interfacial fracture energy G_f is the enclosed area of the bond-slip curve related to these parameters, which can be expressed by the following equation:

$$G_f = \int_0^{+\infty} \tau ds = \int_0^{s_1} \tau ds + \int_{s_1}^{s_2} \tau ds + \int_{s_u}^{+\infty} \tau ds \tag{4}$$

By integrating the shear stress and slip, G_f can be estimated as follows:

$$G_f = \frac{1}{2}\tau_1 s_1 + \frac{1}{2}(\tau_1 + \tau_2)(s_2 - s_1) + \frac{\tau_m}{\omega} \tag{5}$$

in which, the coefficient ω can be expressed by:

$$\omega = \frac{\tau_m}{G_f - \frac{1}{2}\tau_1 s_1 - \frac{1}{2}(\tau_1 + \tau_2)(s_2 - s_1)} \tag{6}$$

For the linear stage I in the strain-slip curve, strain ε_1 can be expressed as follows:

$$\varepsilon(s) = \frac{\varepsilon_1}{s_1} s \tag{7}$$

By considering $\varepsilon = \frac{ds}{dx}$ and $\tau(x) = E_f t_f \frac{d\varepsilon}{ds}\frac{ds}{dx}$, the function of the bond-slip in stage I can be expressed as follows [36]:

$$\tau(s) = E_f t_f \left(\frac{\varepsilon_1}{s_1}\right)^2 s \tag{8}$$

By substituting $s=s_1$, the shear stress τ_1 in stage I can be calculated by:

$$\tau_1 = E_f t_f \frac{\varepsilon_1^{\,2}}{s_1} \tag{9}$$

The function of the bond-slip in stage II can be described by the following equation:

$$\tau(s) = \frac{\tau_2 - \tau_1}{s_2 - s_1} s + \frac{\tau_1 s_2}{s_2 - s_1} - \frac{\tau_2 s_1}{s_2 - s_1} \tag{10}$$

For the linear stage II in the strain-slip curve, the relationship between τ_1, τ_2, ε_1, and ε_2 can be obtained by the previous studies [38, 39]:

$$s_1 = 0.5 s_2 \tag{11}$$

$$\tau_1 = 0.7 \tau_2 \tag{12}$$

Therefore, the coefficient ω can be written as:

$$\omega = \frac{\tau_m}{G_f - 0.55\tau_2 s_2} \tag{13}$$

The elastic-hardening stage II and the nonlinear softening stage III in the strain-slip curve can be expressed by an exponential function to describe the relationship between strain and slip:

$$\varepsilon(s) = \varepsilon_u \left(1 - e^{-\omega s}\right) \tag{14}$$

in which $\varepsilon_u = \sqrt{\frac{2G_f}{E_f t_f}}$ [40]. (15)

All the parameters are determined by the interfacial fracture energy G_f. Therefore, an accurate analytical interfacial fracture energy prediction model is necessary.

5.1 Dynamic interfacial fracture energy

As fracture of concrete was observed varying with loading speeds, and the increased fracture energy is attributed to the increased concrete tensile strength. It has been demonstrated in the previous studies that the interfacial fracture energy is correlated well with the width ratio β_w and tensile strength of concrete f_t [41, 42]. The testing results over 3 m/s showed different failure modes as compared to the results under the loading speed of 3 m/s. Therefore, Equations (16) and (17) were proposed to obtain the dynamic interfacial fracture energy under different strain rates (56.68 s^{-1} corresponds to 1 m/s). To expand the scope of application of the proposed models, a total of 35 dynamic testing results of FRP-to-concrete joints were collected from the previous studies [23, 25]. As the fracture of the adhesive layer was observed in some cases

when the loading speed was over 3 m/s, the strain energy of the adhesive layer (i.e. $f_a^2/2E_a$) should be also incorporated into the proposed model.

$$G_{f,d} = \alpha_1 \beta_w^{\,2} \left(\frac{f_a^{\,2}}{2E_a} \right)^{\alpha_2} \sqrt{TDIF \cdot f_{t,s}} \quad \text{when} \quad 2.5\times10^{-5} s^{-1} < \dot{\varepsilon}_d \le 56.68 s^{-1} \tag{16}$$

$$G_{f,d} = \alpha_3 \beta_w^{\,2} \left(\frac{f_a^{\,2}}{2E_a} \right)^{\alpha_2} \sqrt{TDIF \cdot f_{t,s}} \quad \text{when} \quad 56.68 s^{-1} < \dot{\varepsilon}_d \le 175.65 s^{-1} \tag{17}$$

$$\beta_w = \sqrt{\frac{2 - b_f / b_c}{1 + b_f / b_c}} \tag{18}$$

in which α_1, α_2 and α_3 are the coefficients to be obtained by the data collection, f_a is the tensile strength of adhesive, E_a refers to the elastic modulus of adhesive, b_c represents the width of concrete substrate, and b_f refers to the width of BFRP sheet. The dynamic increase factor for concrete in tension (TDIF) [43] is adopted in the following equations:

$$TDIF = \begin{cases} f_{t,d} / f_{t,s} = 0.26 \log(\dot{\varepsilon}) + 2.06 & \dot{\varepsilon}_d \le 1 s^{-1} \\ f_{t,d} / f_{t,s} = 2 \log(\dot{\varepsilon}) + 2.06 & \text{when} \quad 1 s^{-1} < \dot{\varepsilon}_d \le 2 s^{-1} \\ f_{t,d} / f_{t,s} = 1.443 \log(\dot{\varepsilon}) + 2.223 & 2 s^{-1} < s \le 150 s^{-1} \end{cases} \tag{19}$$

where $f_{t,d}$ is the dynamic tensile strength, $f_{t,s}$ is the static tensile strength, and $\dot{\varepsilon}_d$ is the strain rate.

Table 2. Summary of data collection

Reference	Specimen ID	Adhesive			FRP			Strain rate (s^{-1})	f_t (MPa)	$P_{u,exp}$ (kN)	τ_m (MPa)	G_f (N/mm)
		f_a (MPa)	E_a (GPa)	$f_a^2/2E_a$ (N/mm^2)	E_f (GPa)	t_f (mm)	b_f (mm)					
Shen et al. [23]	L200-D0-1	45.8	2.6	0.403	105	0.242	50	0.61E-3	2.62	11.40	2.95	1.02
	L200-D0-2	45.8	2.6	0.403	105	0.242	50	0.61E-3	2.62	10.80	3.59	0.92
	L200-D0-3	45.8	2.6	0.403	105	0.242	50	0.61E-3	2.62	13.60	-	1.45
	L200-D1-1	45.8	2.6	0.403	105	0.242	50	0.61E-2	3.89	15.00	4.64	1.39
	L200-D1-2	45.8	2.6	0.403	105	0.242	50	0.61E-2	3.89	13.30	5.00	1.23
	L200-D1-3	45.8	2.6	0.403	105	0.242	50	0.61E-2	3.89	12.50	3.89	1.02
	L200-D2-1	45.8	2.6	0.403	105	0.242	50	0.047	4.49	15.50	3.68	0.92
	L200-D2-2	45.8	2.6	0.403	105	0.242	50	0.047	4.49	14.50	5.37	1.46
	L200-D2-3	45.8	2.6	0.403	105	0.242	50	0.047	4.49	13.10	5.39	1.77

	L200-D3-1	45.8	2.6	0.403	105	0.242	50	0.63	5.26	16.20	5.95	1.39
	L200-D3-2	45.8	2.6	0.403	105	0.242	50	0.63	5.26	15.70	5.82	1.23
	L200-D3-3	45.8	2.6	0.403	105	0.242	50	0.63	5.26	15.60	5.49	1.89
Huo et al. [25]	C50-1-S-1	65.0	3.2	0.660	236	0.169	50	1E-5	2.85	13.60	4.05	0.64
	C50-1-S-2	65.0	3.2	0.660	236	0.169	50	1E-5	2.85	11.50	3.50	0.61
	C50-2-S-1	65.0	3.2	0.660	236	0.338	50	1E-5	2.85	18.00	3.28	0.64
	C50-2-S-2	65.0	3.2	0.660	236	0.338	50	1E-5	2.85	14.20	4.25	0.63
	C80-2-S-1	65.0	3.2	0.660	236	0.338	80	1E-5	2.85	17.50	4.74	0.70
	C80-2-S-2	65.0	3.2	0.660	236	0.338	80	1E-5	2.85	18.40	3.47	0.52
	C50-1-D200-1	65.0	3.2	0.660	236	0.169	50	3.12	8.38	15.10	5.40	1.43
	C50-1-D200-2	65.0	3.2	0.660	236	0.169	50	2.67	8.10	17.80	6.93	1.72
	C50-1-D200-3	65.0	3.2	0.660	236	0.169	50	4.56	9.06	16.90	6.02	1.71
	C50-1-D400-1	65.0	3.2	0.660	236	0.169	50	4.10	8.87	24.40	6.39	2.22
	C50-1-D400-2	65.0	3.2	0.660	236	0.169	50	4.90	9.19	18.00	5.47	1.39
	C50-1-D400-3	65.0	3.2	0.660	236	0.169	50	4.70	9.11	16.80	6.45	1.53
	C50-2-D200-1	65.0	3.2	0.660	236	0.169	50	2.09	7.66	20.00	5.58	1.20
	C50-2-D200-2	65.0	3.2	0.660	236	0.169	50	2.05	7.63	21.30	7.33	1.38
	C50-2-D200-3	65.0	3.2	0.660	236	0.169	50	2.62	8.07	27.20	5.22	0.81
	C50-2-D400-1	65.0	3.2	0.660	236	0.338	50	2.63	8.07	24.60	5.49	1.31
	C50-2-D400-2	65.0	3.2	0.660	236	0.338	50	3.13	8.39	33.10	6.21	1.94
	C50-2-D400-3	65.0	3.2	0.660	236	0.338	50	2.02	7.60	29.00	5.47	0.62
	C50-2-D600-2	65.0	3.2	0.660	236	0.338	50	3.59	8.63	24.90	6.56	1.79
	C50-2-D600-2	65.0	3.2	0.660	236	0.338	50	3.65	8.66	24.40	6.20	1.10
	C80-2-D400-1	65.0	3.2	0.660	236	0.338	80	2.55	8.02	27.20	6.48	1.80
	C80-2-D400-1	65.0	3.2	0.660	236	0.338	80	2.92	8.26	27.90	8.13	1.78
	C80-2-D400-1	65.0	3.2	0.660	236	0.338	80	2.10	7.67	21.10	5.68	0.96

Note: $f_t = 0.53\sqrt{f_c}$ (MPa) [44].

Figure 15 shows the relationship between the interfacial fracture energy (G_f) in Z direction and concrete dynamic tensile strength ($f_{t,d}$) in Y direction, adhesive strain energy ($f_a^2/2E_a$) in X direction. After regression analyses, the best-fit coefficients of α_1, α_2 and α_3 are given as 0.53, 0.24 and 0.57 in Equations (20) and (21), respectively. The width β_w can be obtained by Equation (18). Therefore, the expression of the dynamic G_f can be expressed as follows:

$$G_{f,d} = 0.53\beta_w^2 \left(\frac{f_a^2}{2E_a}\right)^{0.24} \sqrt{f_{t,d}} \quad \text{when} \quad 2.5\times10^{-5}s^{-1} < \dot{\varepsilon}_d \le 56.68s^{-1} \tag{20}$$

$$G_{f,d} = 0.57\beta_w^2 \left(\frac{f_a^2}{2E_a}\right)^{0.24} \sqrt{f_{t,d}} \quad \text{when} \quad 56.68s^{-1} < \dot{\varepsilon}_d \le 175.65s^{-1} \tag{21}$$

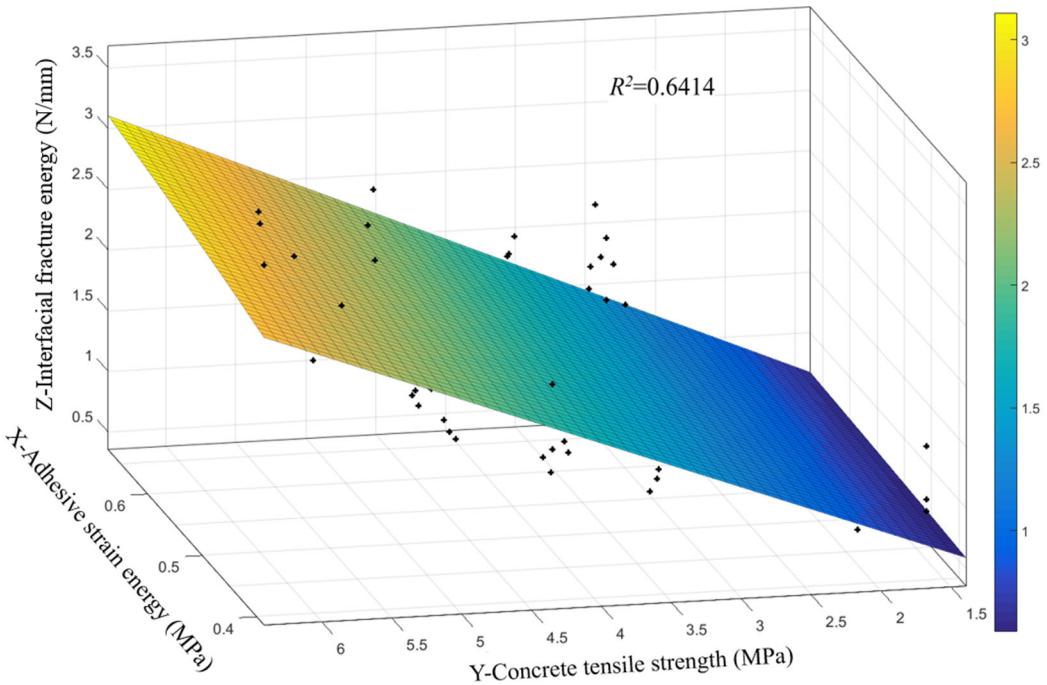

Figure 15. Best-fit coefficients for the interfacial fracture energy

Figure 16 illustrates the contrast between the predicted and experimental fracture energy. It can be seen that the analytical predictions are consistent with the experimental data. The mean ratio between the predicted and experimental results is 1.13 and the corresponding coefficient of variation (COV) is 0.19.

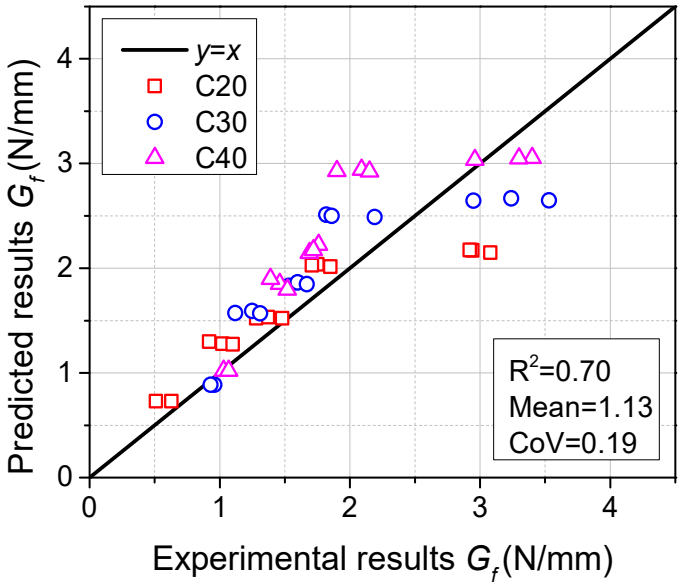

Figure 16. Experimental interfacial fracture energy vs predicted results

360 **5.2 Dynamic ultimate debonding strain**

361 Previous studies [40, 45-47] have proposed some ultimate debonding strain models for
362 structural design purpose based on quasi-static tests, which is used to simulate the FRP
363 debonding caused by the intermediate crack (IC). However, a dynamic debonding strain model
364 has not been proposed yet in the literature. Therefore, an empirical dynamic debonding strain
365 model by incorporating strain rate is proposed herein. A model proposed by Maruyama and
366 Ueda [40] is adopted here to predict the dynamic debonding strain due to this model
367 incorporating both the FRP stiffness interfacial fracture energy and, which can be expressed as
368 follows:

369 $$\varepsilon_u = \sqrt{\frac{2G_f}{E_f t_f}} \tag{22}$$

370 in which ε_u is the ultimate debonding strain, G_f is the interfacial fracture energy, and $E_f t_f$ is FRP
371 stiffness. By substituting the dynamic fracture energy $G_{f,d}$ given in Equations (20) and (21) into
372 Equation (22), the dynamic debonding strain $\varepsilon_{u,d}$ can be obtained and the comparison between
373 the predicted and testing data is plotted in Figure 17. It is clear that the predicted results show
374 good agreement with the testing data due to the mean value of 1.02 and the coefficient of
375 variation (COV) of 0.11.

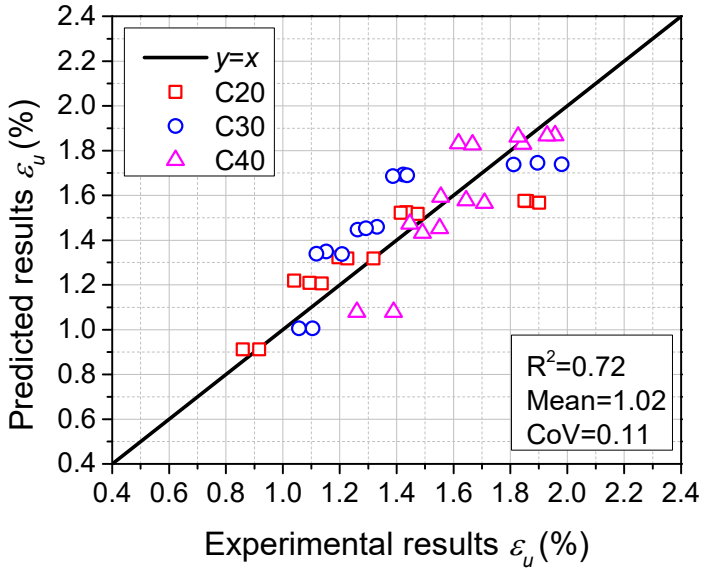

Figure 17. Experimental debonding strain vs predicted results

5.3 Dynamic bond stress and slip

As the fracture of adhesive layer was observed in some cases when the testing velocity was over 3 m/s, the tensile strength of adhesive (f_a) should be one of the factors determining dynamic shear stress of the BFRP-concrete interface. Previous studies [34] have demonstrated that the concrete tensile strength (f_t) width ratio (β_w) and are the key factors in determining the peak shear stress. To expand the scope of application of the proposed dynamic peak shear stress model, the previous test data listed in Table 2 are also selected to conduct the regression analyses. Therefore, three parameters including f_a, β_w, and f_t are incorporated into the following equation to obtain the dynamic peak shear stress $\tau_{m,d}$:

$$\tau_{m,d} = \alpha_4 \left(f_a\right)^{\alpha_5} \beta_w \sqrt{TDIF \cdot f_{t,s}} \tag{23}$$

in which $\tau_{m,d}$ is the dynamic peak shear stress, *TDIF* is the dynamic increases factor for concrete in tension which can be obtained from Equation (19), and $f_{t,s}$ refers to the static concrete tensile strength. After regression analyses, the best-fit coefficients of α_4 and α_5 are 0.23 and 0.53, respectively. Figure 18 shows the relationship between the peak shear stress in *Z* direction with

the concrete tensile strength in Y direction and the adhesive strain energy in X direction. Therefore, the dynamic peak shear stress can be expressed by the following equation:

$$\tau_{m,d} = 0.23\left(f_a\right)^{0.53} \beta_w \sqrt{TDIF \cdot f_{t,s}} \tag{24}$$

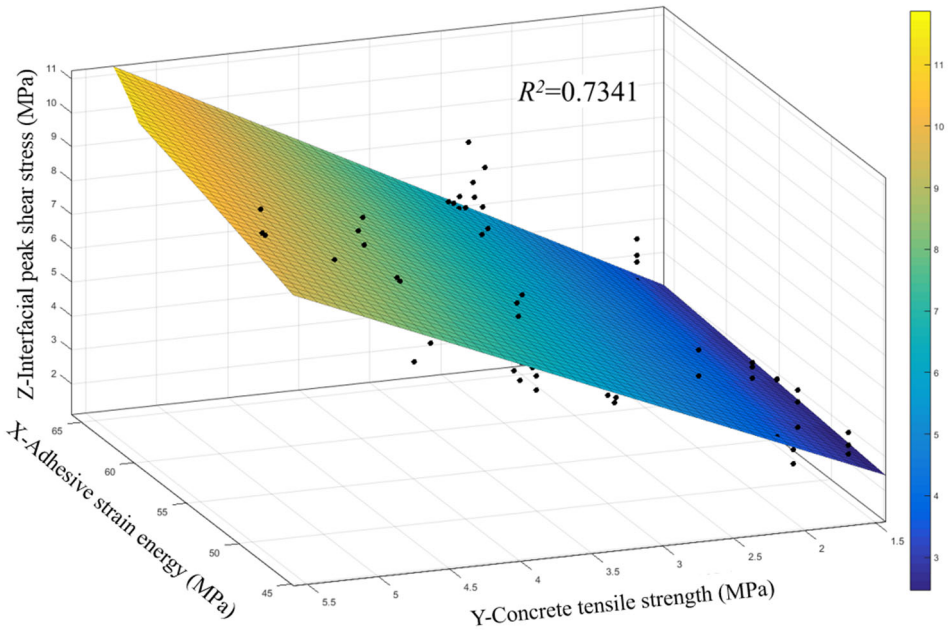

Figure 18. Best-fit coefficients for the peak shear stress

Figure 19 illustrates the comparison between the predicted and experimental results. It is found that the analytical predictions are consistent with the testing results. The mean ratio between the analytical predictions and the testing data is 1.11, and the corresponding coefficient of variation (COV) is 0.22.

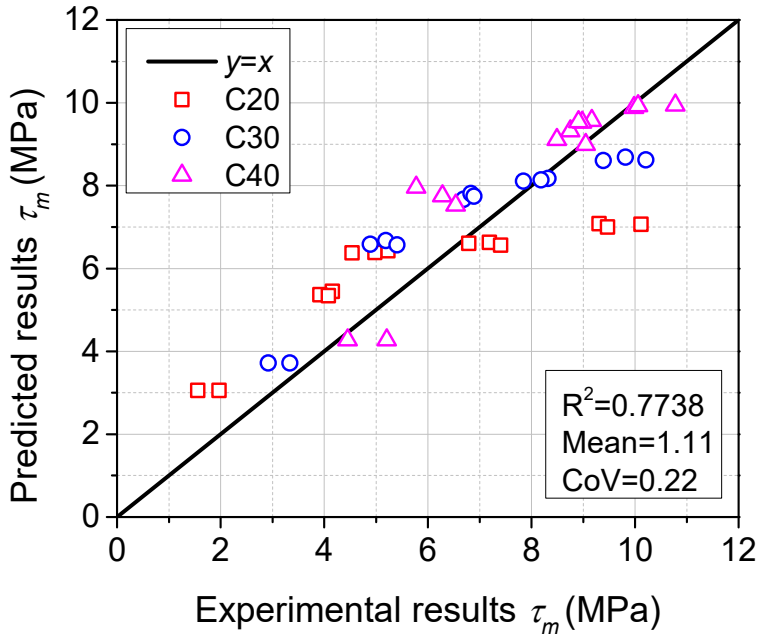

401

402 Figure 19. Experimental peak shear stress (τ_m) vs predicted results

403 According to the testing data, the peak shear slip s_2 at the peak shear stress τ_m decreases with
404 strain rate. However, the adopted peak shear slip s_2 in this study is set as a constant of 0.115
405 mm which is the average of all the tested specimens (i.e., C20, C30 and C40) due to the
406 scattered data, as shown in Figure 20.

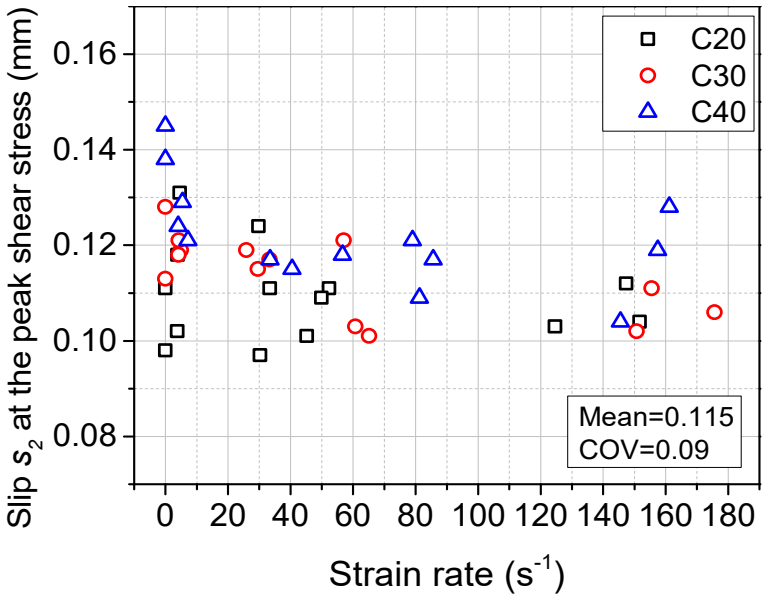

407

408 Figure 20. Shear slip s_2 vs strain rate

5.4 Validation of dynamic bond-slip model

Figure 21 illustrates the comparison between the predicted and experimental strain-slip and bond-slip curves. To demonstrate the reliability of the proposed model, at least four points along the bonded region were selected to track the strain and slip distributions. The distance of 60 mm, 90 mm, 120 mm, 150 mm, and 180 mm shown in the legend refers to the range of strain distribution at five loading stages after the initial debonding stage. The comparison shows that the proposed bond-slip model is in good agreement with the experimental data.

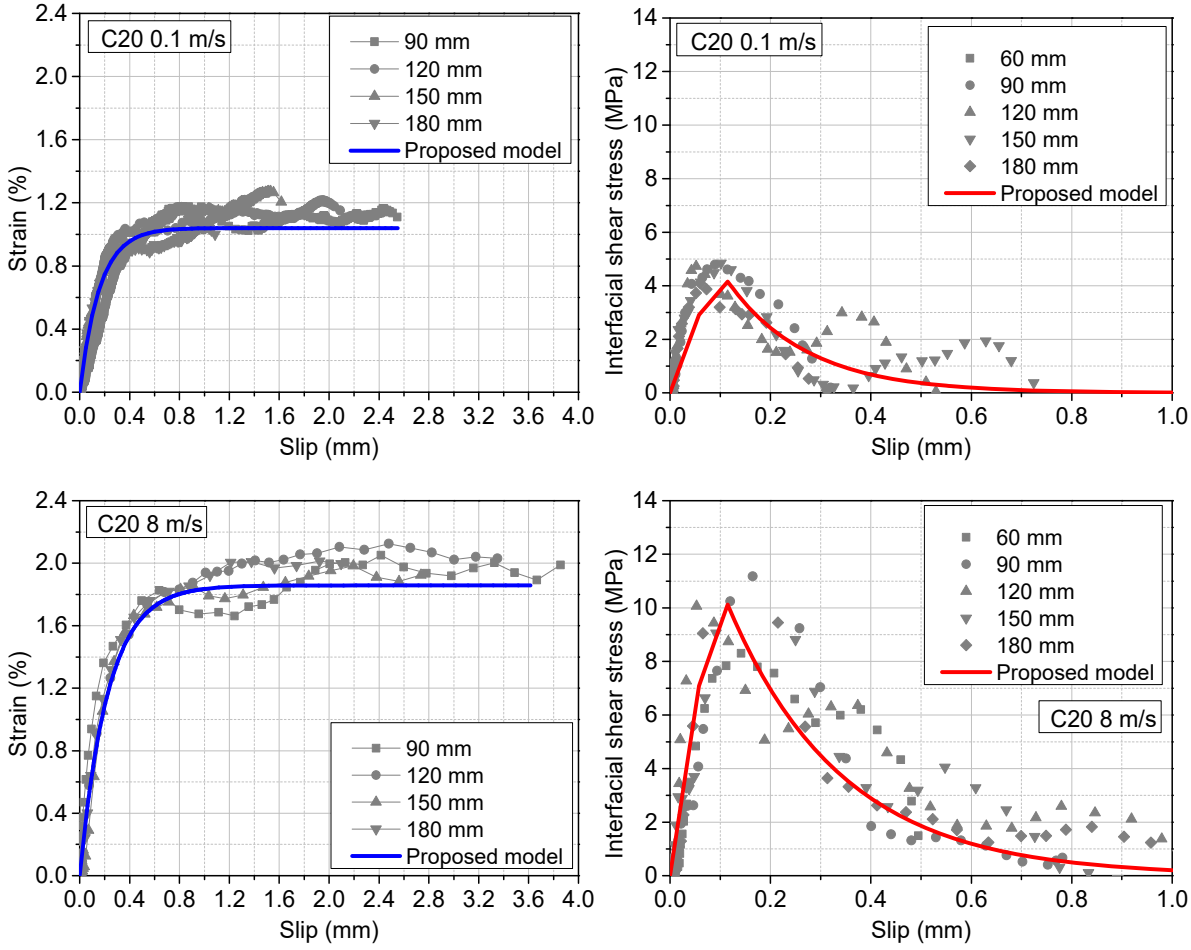

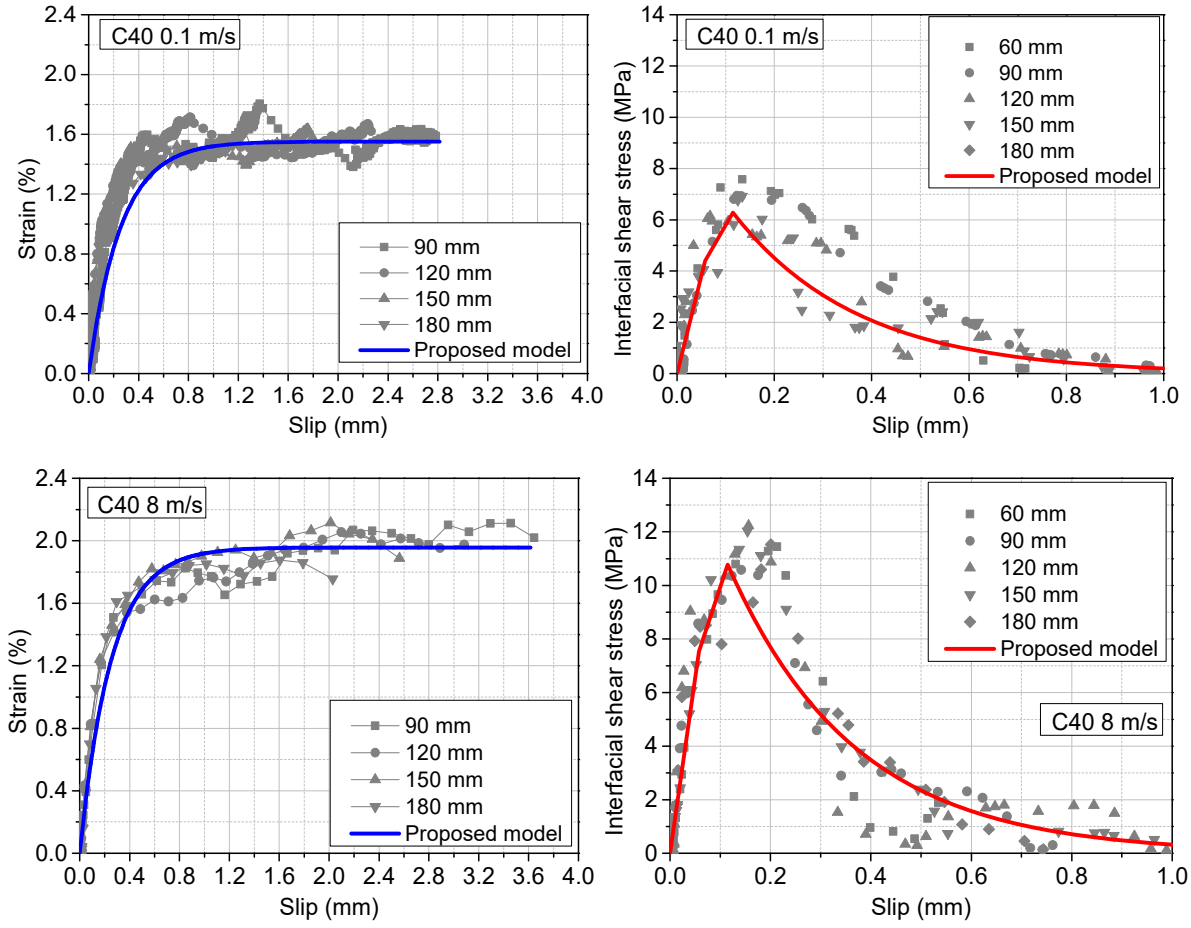

Figure 21. Analytical and experimental strain-slip curves and bond-slip curves

Numerous studies stated that some parameters (i.e. debonding load, shear stress or strain distribution) related to bond behaviour can be estimated by the proposed bond-slip models [34, 48, 49]. Among these parameters, the debonding load and the strain distributions can be directly measured in the test program. Therefore, the validation of the analytical bond-slip model can be carried out via the debonding load and strain distribution. A widely accepted formula for calculating the debonding load can be expressed as follows [15, 37, 50, 51]:

$$P_u = b_f \sqrt{2 E_f t_f G_f} \tag{25}$$

By substituting the dynamic interfacial fracture energy $G_{f,d}$ into Equation (25), the dynamic debonding load can be obtained accordingly. Figure 22 shows the contrast between the predicted and experimental results. It is observed that the predicted debonding load matches

well with the testing data. The mean ratio of the predicted and test results is 1.04 and the corresponding coefficient of variation (COV) is 0.10.

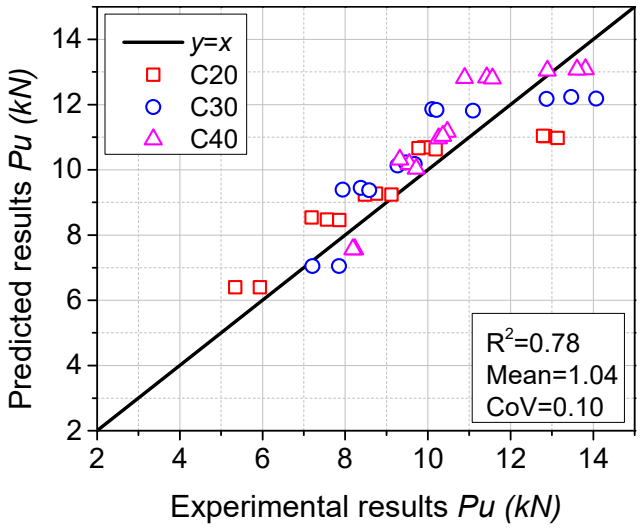

Figure 22. Experimental debonding load (P_u) vs predicted results

6. Conclusions

This study experimentally investigates the effect of concrete strength on the dynamic interfacial bond performance between BFRP and concrete at various strain rates (from 2.50E-5 to 175.65 s^{-1}) through the single-lap shear tests. The following conclusions can be drawn from the test results:

(1) The quasi-static results show that the shear resistance increased with the concrete strength. The interfacial shear resistance increases with the loading rate, and the loading or strain rate sensitivity is concrete strength dependent, specimens made of low-strength concrete is more sensitive to strain rate than those made of higher-strength concrete.

(2) A mixed failure mode was observed in the dynamic tests. The interfacial fracture occurred mainly in concrete layer when loading rate is less than 3 m/s, but occurred in concrete-adhesive interface when loading rate is higher than 3 m/s. When failure occurred in the interface the concrete strength has insignificant effect on the interlayer bonding performance.

(3) Increased strain rate caused the enhancement on the dynamic bond strength. The specimen with the lowest concrete strength experienced the highest strain rate sensitivity with the largest increment ratio of the debonding load. Enhancement up to 129.14% was observed for the specimens with the concrete strength of about 20 MPa while the increment ratio of 63.66% was observed for the ones with the concrete strength of about 40 MPa.

(4) The interfacial fracture energy showed a remarkable increment with the strain rate, especially for the specimens with low concrete strength. Increment ratios of up to 423.63%, 243.42, and 206.96% were observed for specimens made of C20, C30, and C40 concrete, respectively.

(5) The proposed bond-slip model by incorporating the dynamic increase factor of concrete in tension (TDIF) yield good predictions as compared with the testing data.

Acknowledgement

The authors thank the Australian Research Council (ARC LP150100259) for its financial support.

References

[1] Li H, Chen W, Hao H. Dynamic response of precast concrete beam with wet connection subjected to impact loads. Engineering structures. 2019;191:247-63.
[2] Hao Y, Hao H, Zhang X. Numerical analysis of concrete material properties at high strain rate under direct tension. International Journal of Impact Engineering. 2012;39:51-62.
[3] Hao Y, Hao H, Jiang G, Zhou Y. Experimental confirmation of some factors influencing dynamic concrete compressive strengths in high-speed impact tests. Cement and Concrete Research. 2013;52:63-70.
[4] Chen W, Hao H, Jong M, Cui J, Shi Y, Chen L, et al. Quasi-static and dynamic tensile properties of basalt fibre reinforced polymer. Composites Part B: Engineering. 2017;125:123-33.
[5] Zhang H, Smith ST, Gravina RJ, Wang Z. Modelling of FRP-concrete bonded interfaces containing FRP anchors. Construction and Building Materials. 2017;139:394-402.
[6] Smith ST, Teng J. FRP-strengthened RC beams. I: review of debonding strength models. Engineering structures. 2002;24:385-95.
[7] Smith ST, Zhang H, Wang Z. Influence of FRP anchors on the strength and ductility of FRP-strengthened RC slabs. Construction and Building Materials. 2013;49:998-1012.

[8] Chen W, Pham TM, Sichembe H, Chen L, Hao H. Experimental study of flexural behaviour of RC beams strengthened by longitudinal and U-shaped basalt FRP sheet. Composites Part B: Engineering. 2018;134:114-26.
[9] Pham TM, Hao H. Behavior of fiber-reinforced polymer-strengthened reinforced concrete beams under static and impact loads. International Journal of Protective Structures. 2017;8:3-24.
[10] Achintha M, Burgoyne C. Fracture energy of the concrete–FRP interface in strengthened beams. Engineering Fracture Mechanics. 2013;110:38-51.
[11] Subramaniam KV, Carloni C, Nobile L. Width effect in the interface fracture during shear debonding of FRP sheets from concrete. Engineering Fracture Mechanics. 2007;74:578-94.
[12] Vaculik J, Sturm AB, Visintin P, Griffith MC. Modelling FRP-to-substrate joints using the bilinear bond-slip rule with allowance for friction—Full-range analytical solutions for long and short bonded lengths. International journal of solids and structures. 2018;135:245-60.
[13] Mukhtar FM, Faysal RM. A review of test methods for studying the FRP-concrete interfacial bond behavior. Construction and Building Materials. 2018;169:877-87.
[14] Carloni C, Santandrea M, Imohamed IAO. Determination of the interfacial properties of SRP strips bonded to concrete and comparison between single-lap and notched beam tests. Engineering Fracture Mechanics. 2017;186:80-104.
[15] Wu Y-F, Jiang C. Quantification of bond-slip relationship for externally bonded FRP-to-concrete joints. Journal of Composites for Construction. 2013;17:673-86.
[16] Palmieri V, De Lorenzis L. Multiscale modeling of concrete and of the FRP–concrete interface. Engineering Fracture Mechanics. 2014;131:150-75.
[17] ACI. Building code requirements for structural concrete (ACI 318-08) and commentary. Committee American Concrete Institute International Organization for Standardization: American Concrete Institute; 2008.
[18] Oehlers D, Seracino R, Smith S. Design handbook for RC structures retrofitted with FRP and metal plates: Beams and slabs. Standards Publishing Department (of Standards Australia); 2008.
[19] Triantafillou T, Matthys S, Audenaert K, Balázs G, Blaschko M, Blontrock H, et al. Externally bonded FRP reinforcement for RC structures. International Federation for Structural Concrete (fib); 2001.
[20] Council NR. Guide for the design and construction of externally bonded FRP systems for strengthening existing structures. CNR-DT200. 2004.
[21] Yuan C, Chen W, Pham TM, Hao H, Cui J, Shi Y. Strain rate effect on interfacial bond behaviour between BFRP sheets and steel fibre reinforced concrete. Composites Part B: Engineering. 2019:107032.
[22] Shi JW, Zhu H, Wu ZS, Wu G. Experimental study of the strain rate effect of FRP sheet-concrete interface. China Civil Eng J. 2012;45:99-107.
[23] Shen D, Shi H, Ji Y, Yin F. Strain rate effect on effective bond length of basalt FRP sheet bonded to concrete. Construction and Building Materials. 2015;82:206-18.
[24] Caggiano A, Martinelli E, Schicchi DS, Etse G. A modified Duvaut-Lions zero-thickness interface model for simulating the rate-dependent bond behavior of FRP-concrete joints. Composites Part B: Engineering. 2018;149:260-7.
[25] Huo J, Liu J, Dai X, Yang J, Lu Y, Xiao Y, et al. Experimental study on dynamic behavior of CFRP-to-concrete interface. Journal of Composites for Construction. 2016;20:04016026.
[26] Salimian MS, Mostofinejad D. Experimental Evaluation of CFRP-Concrete Bond Behavior under High Loading Rates Using Particle Image Velocimetry Method. Journal of Composites for Construction. 2019;23:04019010.

528 [27] Yuan C, Chen W, Pham TM, Hao H. Effect of aggregate size on bond behaviour between
529 basalt fibre reinforced polymer sheets and concrete. Composites Part B: Engineering.
530 2019;158:459-74.
531 [28] Yuan C, Chen W, Pham TM, Hao H. Bond behaviour between hybrid fiber reinforced
532 polymer sheets and concrete. Construction and Building Materials. 2019;210:93-110.
533 [29] Yuan C, Chen W, Pham TM, Hao H. Bond behavior between basalt fibres reinforced
534 polymer sheets and steel fibres reinforced concrete. Engineering structures. 2018;176:812-24.
535 [30] Li X, Chen J-F, Lu Y, Yang Z. Modelling static and dynamic FRP-concrete bond
536 behaviour using a local concrete damage model. Advances in Structural Engineering.
537 2015;18:45-58.
538 [31] Shen D, Ji Y, Yin F, Zhang J. Dynamic bond stress-slip relationship between basalt FRP
539 sheet and concrete under initial static loading. Journal of Composites for Construction.
540 2015;19:04015012.
541 [32] Cui J, Hao H, Shi Y. Discussion on the suitability of concrete constitutive models for high-
542 rate response predictions of RC structures. International Journal of Impact Engineering.
543 2017;106:202-16.
544 [33] Hao Y, Hao H. Dynamic compressive behaviour of spiral steel fibre reinforced concrete
545 in split Hopkinson pressure bar tests. Construction and Building Materials. 2013;48:521-32.
546 [34] Wu Y-F, Xu X-S, Sun J-B, Jiang C. Analytical solution for the bond strength of externally
547 bonded reinforcement. Composite Structures. 2012;94:3232-9.
548 [35] Sun W, Peng X, Liu HF, Qi HP. Numerical studies on the entire debonding propagation
549 process of FRP strips externally bonded to the concrete substrate. Construction and Building
550 Materials. 2017;149:218-35.
551 [36] Biscaia HC, Chastre C, Borba IS, Silva C, Cruz D. Experimental evaluation of bonding
552 between CFRP laminates and different structural materials. Journal of Composites for
553 Construction. 2015;20:04015070.
554 [37] Laura De Lorenzis B, Antonio N. Bond of fiber-reinforced polymer laminates to concrete.
555 Mater J. 2001;98:256-64.
556 [38] Yuan H, Lu X, Hui D, Feo L. Studies on FRP-concrete interface with hardening and
557 softening bond-slip law. Composite Structures. 2012;94:3781-92.
558 [39] Woo S-K, Lee Y. Experimental study on interfacial behavior of CFRP-bonded concrete.
559 KSCE Journal of Civil Engineering. 2010;14:385-93.
560 [40] Maruyama K, Ueda T. JSCE recommendations for upgrading of concrete structures with
561 use of continuous fiber sheets. FRP Composites in Civil Engineering Proceedings of the
562 International Conference on FRP composites in Civil EngineeringHong Kong Institution of
563 Engineers, Hong Kong Institution of Steel Construction2001.
564 [41] Pan J, Leung CK. Effect of concrete composition on FRP/concrete bond capacity. Journal
565 of Composites for Construction. 2007;11:611-8.
566 [42] Toutanji H, Saxena P, Zhao L, Ooi T. Prediction of interfacial bond failure of FRP–
567 concrete surface. Journal of Composites for Construction. 2007;11:427-36.
568 [43] Hao Y, Hao H. Influence of the concrete DIF model on the numerical predictions of RC
569 wall responses to blast loadings. Engineering structures. 2014;73:24-38.
570 [44] Lu XZ, Teng JG, Ye LP, Jiang JJ. Bond–slip models for FRP sheets/plates bonded to
571 concrete. Engineering structures. 2005;27:920-37.
572 [45] Teng J, Smith ST, Yao J, Chen JF. Intermediate crack-induced debonding in RC beams
573 and slabs. Construction and Building Materials. 2003;17:447-62.
574 [46] Said H, Wu Z. Evaluating and proposing models of predicting IC debonding failure.
575 Journal of Composites for Construction. 2008;12:284-99.

576 [47] Elsanadedy H, Abbas H, Al-Salloum Y, Almusallam T. Prediction of intermediate crack
577 debonding strain of externally bonded FRP laminates in RC beams and one-way slabs. Journal
578 of Composites for Construction. 2014;18:04014008.
579 [48] Pellegrino C, Tinazzi D, Modena C. Experimental study on bond behavior between
580 concrete and FRP reinforcement. Journal of Composites for Construction. 2008;12:180-9.
581 [49] Dai J, Ueda T, Sato Y. Bonding characteristics of fiber-reinforced polymer sheet-concrete
582 interfaces under dowel load. Journal of Composites for Construction. 2007;11:138-48.
583 [50] Wan B, Jiang C, Wu Y-F. Effect of defects in externally bonded FRP reinforced concrete.
584 Construction and Building Materials. 2018;172:63-76.
585 [51] Biscaia HC, Chastre C, Silva MA. Linear and nonlinear analysis of bond-slip models for
586 interfaces between FRP composites and concrete. Composites Part B: Engineering.
587 2013;45:1554-68.

588